LETTER

https://doi.org/10.1038/s41586-019-1471-1

Locally renewing resident synovial macrophages provide a protective barrier for the joint

Stephan Culemann[1,2,11], Anika Grüneboom[1,2,11], José Ángel Nicolás-Ávila[3], Daniela Weidner[1,2], Katrin Franziska Lämmle[1,2], Tobias Rothe[1,2], Juan A. Quintana[3], Philipp Kirchner[4], Branislav Krljanac[5], Martin Eberhardt[6], Fulvia Ferrazzi[4], Elke Kretzschmar[7], Martin Schicht[7], Kim Fischer[1], Kolja Gelse[8], Maria Faas[1,2], René Pfeifle[1,2], Jochen A. Ackermann[1,2], Milena Pachowsky[8], Nina Renner[8], David Simon[1], Reiner F. Haseloff[9], Arif B. Ekici[4], Tobias Bäuerle[10], Ingolf E. Blasig[9], Julio Vera[6], David Voehringer[5], Arnd Kleyer[1], Friedrich Paulsen[7], Georg Schett[1], Andrés Hidalgo[3] & Gerhard Krönke[1,2]*

Macrophages are considered to contribute to chronic inflammatory diseases such as rheumatoid arthritis[1]. However, both the exact origin and the role of macrophages in inflammatory joint disease remain unclear. Here we use fate-mapping approaches in conjunction with three-dimensional light-sheet fluorescence microscopy and single-cell RNA sequencing to perform a comprehensive spatiotemporal analysis of the composition, origin and differentiation of subsets of macrophages within healthy and inflamed joints, and study the roles of these macrophages during arthritis. We find that dynamic membrane-like structures, consisting of a distinct population of CX_3CR1^+ tissue-resident macrophages, form an internal immunological barrier at the synovial lining and physically seclude the joint. These barrier-forming macrophages display features that are otherwise typical of epithelial cells, and maintain their numbers through a pool of locally proliferating CX_3CR1^- mononuclear cells that are embedded into the synovial tissue. Unlike recruited monocyte-derived macrophages, which actively contribute to joint inflammation, these epithelial-like CX_3CR1^+ lining macrophages restrict the inflammatory reaction by providing a tight-junction-mediated shield for intra-articular structures. Our data reveal an unexpected functional diversification among synovial macrophages and have important implications for the general role of macrophages in health and disease.

The healthy synovial cavity is a fluid-containing sterile space that lacks immune cell trafficking. During inflammatory joint diseases such as rheumatoid arthritis, increasing numbers of mononuclear phagocytes and synovial fibroblasts are thought to contribute to an expanding synovial pannus that drives the destruction of articular cartilage and bone[2–4]. Previous work that addressed the role of monocytes and macrophages during arthritis accordingly suggested that these cells promote both the onset and the progression of joint inflammation[1,5–8], a scenario that has substantially shaped our current view on the role of these cells during inflammatory disease in general.

More recent studies have questioned the concept that macrophages uniformly originate from blood monocytes, and have shown that certain subsets of macrophages populate organs during early development and subsequently self-sustain their numbers in a monocyte-independent manner[9–12]. Individual subsets of such resident macrophages have distinct transcriptional and epigenetic signatures, which suggests that they have highly specialized and tissue-specific functions[13–16]. These recent insights prompted us to question prevailing paradigms and to revisit the origin and function of synovial macrophages during homeostasis and inflammatory joint disease.

CX_3CR1 is a chemokine receptor that is specifically used by mononuclear phagocytes and their precursors[11]. To visualize the spatial distribution of CX_3CR1^+ macrophages and macrophages originating from CX_3CR1^+ precursors, respectively, we performed confocal immunofluorescence microscopy and three-dimensional light-sheet fluorescence microscopy of optically cleared knee joints in *Cx3cr1*^{cre}*Rosa26*(*R26*)-*tdTomato* mice (Fig. 1a, b, Supplementary Video 1). This approach revealed membrane-like structures of synovial tdTomato$^+$ macrophages that formed a dense physical barrier between the synovial capillary network and the intra-articular space, thereby secluding the joint space from the exterior (Fig. 1b, c, Supplementary Videos 2–4). Analysis of *ColVI*^{cre}*R26-tdTomato* reporter mice showed that these macrophages formed the uppermost cellular layer and covered the lining of collagen VI-expressing synovial fibroblasts (Extended Data Fig. 1a). In *Cx3cr1*^{GFP} mice, we confirmed that such membrane-forming lining macrophages selectively expressed CX_3CR1, stained positive for CD68 and F4/80, and constituted 40% of the total synovial macrophages under steady-state conditions. By contrast, interstitial synovial macrophages did not express CX_3CR1 (Extended Data Fig. 1a, b).

Next, we studied the response of macrophages during K/BxN serum-transfer arthritis (STA) and collagen-induced arthritis as mouse models of rheumatoid arthritis. The onset of inflammation resulted in a rapid change in the morphology and spatial orientation of CX_3CR1^+ macrophages that suddenly abrogated cell–cell contacts (Fig. 1d, Extended Data Fig. 1c–h, Supplementary Videos 5–7). Simultaneously, collagen VI-expressing fibroblasts started occupying the synovial surface (Extended Data Fig. 1f) and $Ly6G^+$ polymorphonuclear leucocytes (PMNs) appeared within the intra-articular space. Dying PMNs were subsequently removed by lining macrophages that had acquired a palisade-like shape (Fig. 1d, Extended Data Fig. 1c–e).

During embryonic development, we detected CX_3CR1^+ synovial lining macrophages by embryonic day (E)15.5 and E16.5, which indicates that synovial macrophage precursors derive from early embryonic haematopoiesis (Extended Data Fig. 2a). Adult parabiotic wild-type mice that shared circulation with *Cx3cr1*^{GFP} mice displayed chimeric myeloid cell populations within the peripheral blood, but no detectable chimerism among CX_3CR1^+ synovial lining macrophages (Fig. 2a). These data suggested that, in the adult mouse, this subset of macrophages maintained its numbers independent of blood monocytes. Analysis of Ki67 expression revealed no signs of proliferation within

[1]Department of Internal Medicine 3 - Rheumatology and Immunology, Universitätsklinikum Erlangen and Friedrich-Alexander University Erlangen-Nürnberg (FAU), Erlangen, Germany. [2]Nikolaus Fiebiger Center of Molecular Medicine, Universitätsklinikum Erlangen and Friedrich-Alexander University Erlangen-Nürnberg (FAU), Erlangen, Germany. [3]Area of Cell and Developmental Biology, Centro Nacional de Investigaciones Cardiovasculares Carlos III, Madrid, Spain. [4]Institute of Human Genetics, Universitätsklinikum Erlangen and Friedrich-Alexander University Erlangen-Nürnberg (FAU), Erlangen, Germany. [5]Department of Infection Biology, Universitätsklinikum Erlangen, Friedrich Alexander University Erlangen-Nürnberg (FAU), Erlangen, Germany. [6]Laboratory of Systems Tumor Immunology, Department of Dermatology, Universitätsklinikum Erlangen and Friedrich-Alexander University Erlangen-Nürnberg (FAU), Erlangen, Germany. [7]Department of Functional and Clinical Anatomy, Friedrich-Alexander University Erlangen-Nürnberg (FAU), Erlangen, Germany. [8]Department of Trauma Surgery, Universitätsklinikum Erlangen, Friedrich Alexander University Erlangen-Nürnberg (FAU), Erlangen, Germany. [9]Leibniz Research Institute of Molecular Pharmacology, Berlin, Germany. [10]Institute of Radiology, PIPE (Preclinical Imaging Platform Erlangen), Universitätsklinikum Erlangen and Friedrich-Alexander University Erlangen-Nürnberg (FAU), Erlangen, Germany. [11]These authors contributed equally: Stephan Culemann, Anika Grüneboom. *e-mail: gerhard.kroenke@uk-erlangen.de

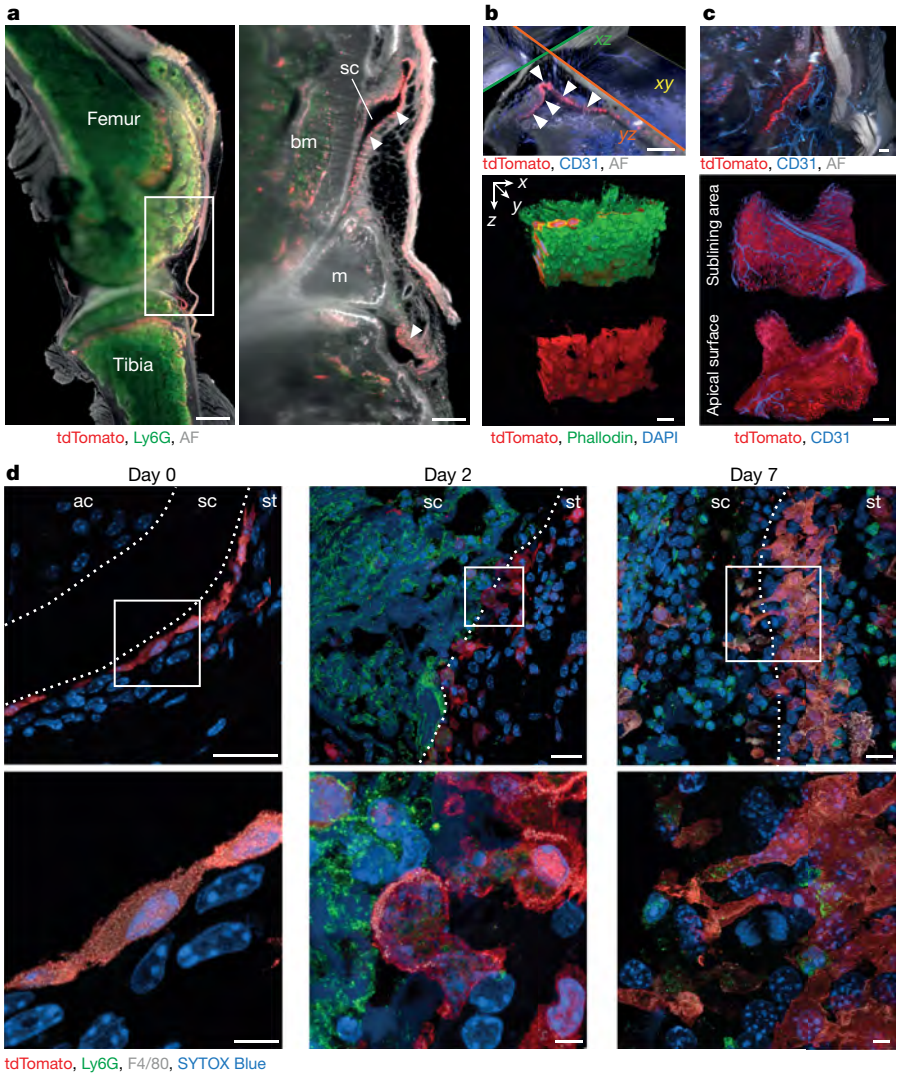

Fig. 1 | CX_3CR1^+ lining macrophages form a dynamic membrane-like structure around the synovial cavity. a–d, Representative 3D light-sheet fluorescence microscopy (LSFM) and confocal laser scanning microscopy (CLSM) of knee joints of *Cx3cr1*^{cre}*R26-tdTomato* mice (LSFM, $n = 10$; CLSM, $n = 3$). **a**, The spatial localization of synovial macrophages (tdTomato, red) and PMNs (Ly6G, green) are shown during steady state (autofluorescence (AF), grey). Arrowheads indicate the localization of the macrophage layer (tdTomato, red) at the border of the synovial cavity (sc). bm, bone marrow; m, meniscus. Scale bars, 500 μm (left), 100 μm (right). **b**, Top, LSFM analysis of the spatial arrangement of the synovial macrophage lining (tdTomato, red; arrowheads) and $CD31^+$ endothelial cells (blue) along the synovial cavity in three dimensions (AF, grey). Scale bars, 100 μm. Bottom, high-resolution 3D reconstruction of a processed CLSM scan of the synovial macrophage lining (tdTomato, red; Phalloidin, green; DAPI, blue). Scale bar, 10 μm. **c**, Three-dimensional reconstruction of LSFM data of the spatial orientation of synovial macrophages (tdTomato, red) and $CD31^+$ endothelial cells (blue) of the synovial capillary network (AF, grey). Scale bars, 100 μm. **d**, CLSM of the synovial membrane visualizing synovial macrophages (tdTomato, red) and PMNs (Ly6G, green) at the indicated time points upon the induction of K/BxN STA. Scale bars, 20 μm (top), 5 μm (bottom). ac, articular cartilage; st, synovial tissue.

the layer of CX_3CR1^+ lining macrophages (Fig. 2b), thus raising questions regarding their mechanism of repopulation and turnover. Notably, we detected clusters of proliferating $Ki67^+CX_3CR1^-$ interstitial cells within deeper layers of the synovial tissue (Fig. 2b). The Ki67 signal decreased in upper cellular layers in which CX_3CR1 expression simultaneously increased, suggestive of a pool of proliferating CX_3CR1^- interstitial macrophages that contributed to the pool of CX_3CR1^+ lining macrophages. Antibody-mediated staining of the M-CSF receptor (CSF1R) within the synovial tissue, as well as mice expressing a *Csf1r* promoter-driven GFP (*Csf1r*^{GFP} mice), showed that only CX_3CR1^- interstitial macrophages—and not CX_3CR1^+ lining macrophages—expressed CSF1R on their surface (Extended Data Fig. 2b, c). We therefore crossed *R26-tdTomato* mice with mice expressing a *Csf1r* promoter-driven and tamoxifen-dependent Cre recombinase (*Csf1r*^{creER}*R26-tdTomato*), an approach that enabled fate mapping of all cells that had expressed CSF1R at a certain developmental stage. After the start of tamoxifen treatment, lining CX_3CR1^+ macrophages acquired tdTomato expression only gradually over time, reaching 65% $tdTomato^+$ cells after 6 weeks. These data indicate that CX_3CR1^+ lining macrophages have a half-life of approximately five weeks and did indeed originate from local CSF1R-expressing CX_3CR1^- interstitial macrophages (Fig. 2c, d).

Additional characterization of parabiotic wild-type mice that shared circulation with *DsRed*-transgenic mice confirmed that, during steady state, both CX_3CR1^+ lining macrophages and CX_3CR1^- interstitial macrophages maintained their numbers independent of monocytes (Extended Data Fig. 2d–i). Although blood-derived monocytes contributed to the pool of synovial macrophages during STA, this influx only partially accounted for the inflammation-induced increase in macrophage numbers (Fig. 2e, f, Extended Data Fig. 2j, k), which indicates an increased proliferative response of tissue-resident synovial macrophages during arthritis. To differentiate between the proliferation of CX_3CR1^- interstitial macrophages and that of CX_3CR1^+ lining macrophages, we crossed *R26-tdTomato* mice with mice that express

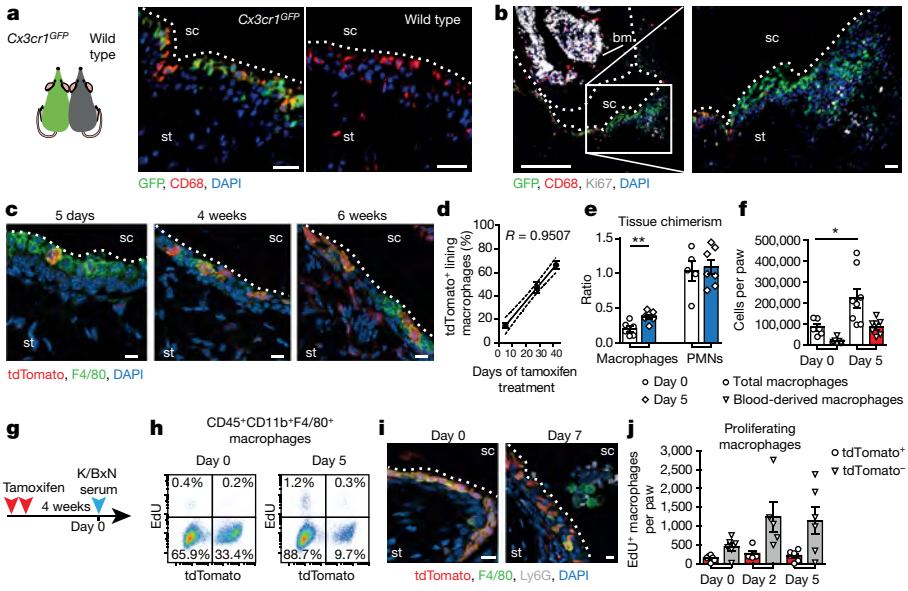

Fig. 2 | CX_3CR1^+ lining macrophages repopulate locally from CSF1R-expressing interstitial macrophages. a, Bright-field fluorescence microscopy of the synovial membrane of knees of *Cx3cr1*^{GFP} (left) and corresponding parabiotic wild-type mice (right) ($n = 3$) after 6 weeks of parabiosis (GFP, green; CD68, red; DAPI, blue). Scale bars, 25 μm. **b**, Bright-field fluorescence microscopy of the synovial membrane of knees of *Cx3cr1*^{GFP} mice ($n = 3$) determining proliferation among subsets of macrophages (GFP, green; Ki67, white; CD68, red; DAPI, blue). Scale bars, 250 μm (left), 25 μm (right). **c**, **d**, CLSM (**c**) and quantification (**d**) of tdTomato$^+$ macrophages within the synovial lining of *Csf1r*^{creER}*R26-tdTomato* mice at the indicated time points during tamoxifen treatment. $n = 3$ for each time point. In **c**, tdTomato, red; F4/80, green; DAPI, blue. Scale bars, 10 μm. In **d**, the dotted line represents the 95% confidence band of linear regression. **e**, Synovial tissue chimerism ratio of CD45$^+$CD11b$^+$F4/80$^+$ macrophages and Ly6G$^+$ PMNs of parabiotic *DsRed*/wild-type mice after 6 weeks of parabiosis under steady-state conditions (day 0: macrophage, $n = 6$; PMNs, $n = 5$) and 5 days after induction of K/BxN STA (macrophage, $n = 7$; PMNs, $n = 7$). Data are mean ± s.e.m.; two-tailed Student's *t*-test, $^{**}P = 0.004$. **f**, Absolute numbers of total and blood-derived CD45$^+$CD11b$^+$F4/80$^+$ macrophages under steady-state conditions (day 0: total macrophages, $n = 6$; blood-derived macrophages, $n = 6$) and at day 5 of STA (total macrophages, $n = 8$; blood-derived macrophages, $n = 7$). Data are mean ± s.e.m.; two-tailed Student's *t*-test, $^*P = 0.0261$. **g**–**j**, Synovial tissue of *Cx3cr1*^{creER}*R26-tdTomato* mice was analysed 4 weeks after tamoxifen pulse to determine EdU incorporation (EdU pulse 4 h before collection) into CD45$^+$CD11b$^+$F4/80$^+$ macrophages (**h**) and tdTomato expression within the synovial lining at indicated time points upon the induction of STA (F4/80, white; Ly6G, green; tdTomato, red; DAPI, blue) (**i**). Scale bars, 10 μm. **j**, Quantification of total proliferating EdU$^+$ tdTomato$^+$ and tdTomato$^-$ macrophages from the paws of tamoxifen-pulsed *Cx3cr1*^{creER}*R26-tdTomato* mice at day 0 ($n = 6$), 2 ($n = 5$), and 5 ($n = 6$) after the induction of STA. Data are mean ± s.e.m.

a gene encoding a tamoxifen-dependent Cre recombinase within the *Cx3cr1* locus (*Cx3cr1*^{creER}*R26-tdTomato* mice). Tamoxifen treatment resulted in selective and continuous expression of tdTomato in the layer of CX_3CR1^+ synovial lining macrophages. A proportion of CX_3CR1^+ blood monocytes was initially marked after systemic tamoxifen treatment, but became rapidly replaced by newly generated tdTomato$^-$ monocytes. Induction of arthritis four weeks after a systemic tamoxifen pulse or a local tamoxifen injection enabled selective fate mapping of tissue-resident CX_3CR1^+ lining macrophages during steady state and inflammation, and therefore enabled discrimination from interstitial or monocyte-derived macrophages (Fig. 2g–i, Extended Data Fig. 3a–f). In conjunction with 5-ethynyl-2′-deoxyuridine (EdU) labelling, this approach confirmed that—at the onset of arthritis—CX_3CR1^+ lining macrophages changed their spatial orientation and morphology but maintained their position, and neither proliferated nor changed in number. By contrast, CX_3CR1^- macrophages rapidly proliferated and accordingly increased in number (Fig. 2h–j, Extended Data Fig. 3f–h).

Bulk RNA sequencing of sorted steady-state CX_3CR1^+ lining macrophages and CX_3CR1^- interstitial synovial macrophages showed that they did indeed represent distinct macrophage populations, both of which are only distantly related to bone-marrow-derived macrophages (Fig. 3a, b, Extended Data Fig. 4a–e). In addition, unbiased molecular profiling of total synovial CD45$^+$CD11b$^+$Ly6G$^-$ mononuclear phagocytes by single-cell RNA sequencing (scRNA-seq) confirmed the presence of the defined cluster of differentiated CX3CR1$^+$ lining macrophages, which co-expressed immune-genes such as *Trem2* or *Vsig4* (Fig. 3c, d, Supplementary Table 1). However, scRNA-seq also revealed an additional degree of heterogeneity among CX_3CR1^- interstitial macrophages. A large number of interstitial CX_3CR1^- macrophages expressed relatively high levels mRNAs encoding MHCII and aquaporin (AQP1), whereas another population of interstitial CX_3CR1^- macrophages was characterized by the expression of *Retnla* (which encodes RELM-α) and additional genes—such as *Mrc1* or *Cd163*—that have previously been implicated in the alternative activation of macrophages (Fig. 3c, d). There was also a smaller population of interstitial *Stmn1*-expressing CX_3CR1^- macrophages that were clustered primarily as a result of their high expression of cell-cycle-associated genes such as *Cdk1*; this suggests that they were not a distinct cellular population but instead were proliferating interstitial MHCII$^+$ and AQP1$^+$$CX_3CR1^-$ macrophages (Fig. 3c, d, Extended Data Fig. 4f, g). Pseudotime analyses indicated that both RELM-α$^+$ macrophages and CX_3CR1^+ lining macrophages were differentiated macrophages that originated from the cluster of proliferating MHCII$^+$$CX_3CR1^-$ interstitial macrophages (Extended Data Fig. 4h–j). This analysis additionally suggested that the initial proliferation of interstitial MHCII$^+$$CX_3CR1^-$ macrophages was followed by an upregulation of mRNAs encoding the transcription factors MAFB and MAF, which have previously been shown to interfere with macrophage proliferation[17] (Extended Data Fig. 4j). Fate mapping in tamoxifen-treated *Csf1r*^{creER}*R26-tdTomato* mice confirmed that—in accordance with this pseudotime model—interstitial MHCII$^+$ macrophages immediately responded with the expression of tdTomato, whereas interstitial RELM-α$^+$ macrophages and CX_3CR1^+ lining macrophages only gradually acquired tdTomato expression over time (Extended Data Fig. 4k–m). Analysis of *Retnla*^{cre}*R26-tdTomato* mice and *Cx3cr1*^{creER}*R26-tdTomato* mice indicated that both subsets of macrophages represented the end stages of synovial macrophage differentiation, because we detected very few

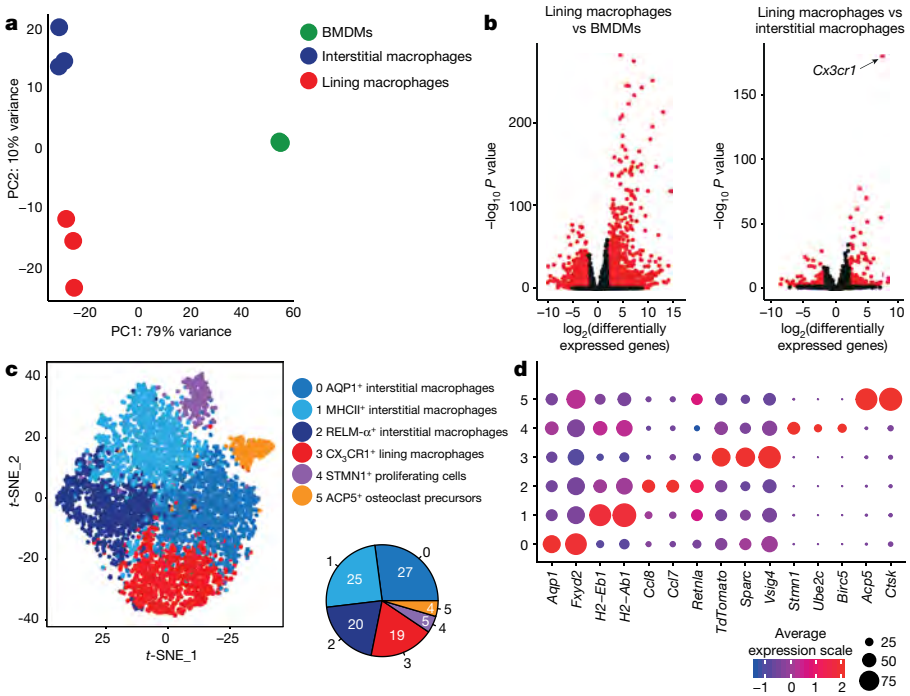

Fig. 3 | Transcriptional profiling of synovial macrophage subsets. **a**, **b**, Principal component (PC) analysis (**a**) and differential gene expression (**b**) of sorted synovial CD45$^+$CD11b$^+$F4/80$^+$GFP$^+$ lining macrophages and CD45$^+$CD11b$^+$F4/80$^+$GFP$^-$ interstitial macrophages of *Cx3cr1*^{GFP} mice, and in vitro-cultured bone-marrow-derived macrophages (BMDMs) of C57BL/6 mice during steady state ($n = 3$) after bulk RNA sequencing. Differential expression analysis was performed with DESeq2. The Wald test was used to calculate two-sided *P* values; adjustment for multiple comparisons was performed with the Benjamini–Hochberg method. **c**, **d**, *t*-distributed stochastic neighbour embedding (*t*-SNE) scRNA-seq profiles (**c**) and dot plot (**d**) showing the average expression level of selected marker genes of the respective clusters of sorted synovial CD45$^+$CD11b$^+$Ly6G$^-$ mononuclear phagocytes of *Cx3cr1*^{creER}*R26-tdTomato* mice analysed 4 weeks after tamoxifen pulse during steady-state conditions ($n = 7{,}362$ cells). The average expression level corresponds to all cells expressing the certain gene. The size of the dots represents the percentage of cells expressing a gene.

cells that had expressed RELM-α within the synovial lining (Extended Data Fig. 4n) or cells that had expressed CX$_3$CR1 within the interstitial synovial tissue (Fig. 2i). As expected, continuous diphtheria toxin (DT)-mediated depletion of CSF1R-expressing synovial macrophages in *Lysm*^{cre}*CD115DTR* mice resulted in the complete depletion of interstitial MHCII$^+$ macrophages, whereas the density of CX$_3$CR1$^+$ lining macrophages decreased only slowly with time. Cessation of DT treatment led to rapid repopulation of the pool of proliferating interstitial MHCII$^+$ macrophages, whereas the repopulation of CX$_3$CR1$^+$ lining macrophages was delayed (Extended Data Fig. 4o, p). Together, these experimental datasets supported the scRNA-seq-based pseudotime model of a dynamic continuum within resident synovial macrophages, in which proliferating MHCII$^+$CX$_3$CR1$^-$ interstitial macrophages further differentiate either into CX$_3$CR1$^+$ lining macrophages or RELM-α$^+$ interstitial macrophages (Extended Data Fig. 5q).

scRNA-seq confirmed that the onset of STA resulted in the appearance of additional clusters of mononuclear phagocytes that displayed the signature of monocyte-derived macrophages; these clusters expanded during the progression of arthritis. These mostly *Ccr2*- and *Ly6c2*-expressing cells displayed a pro-inflammatory activation profile, including the expression of *Il1b* (Extended Data Fig. 5a, b and Supplementary Table 2). Tamoxifen-pulsed *Cx3cr1*^{creER}*R26-tdTomato* mice enabled us to fate map tdTomato-expressing CX$_3$CR1$^+$ lining macrophages within the generated scRNA-seq datasets throughout the course of STA. This analysis showed that—despite their increasingly inflammatory microenvironment—lining macrophages stably maintained their immune-regulatory phenotype, including the expression of *Trem2* and of high levels of receptors that mediate the clearance of apoptotic cells, such as *Axl* and *Mfge8* (Extended Data Fig. 5b, c). A comparison of available scRNA-seq datasets from human rheumatoid arthritis synovium[8] showed that the expression profiles of two of four recently described subsets of human synovial monocytes (SC-M2 and SC-M3) matched the profiles of mouse resident synovial macrophages, whereas the other two subsets of human synovial monocytes (SC-M1 and SC-M4) resembled mouse monocyte-derived synovial macrophages (Extended Data Fig. 5d).

Notably, CX$_3$CR1$^+$ lining macrophages also displayed features that are otherwise typical of barrier-forming epithelial cells, and expressed mRNAs encoding tight-junction proteins such as JAM1 (*F11r*), ZO-1 (*Tjp1*) and claudin 5 (*Cldn5*), as well as genes involved in planar cell polarity, including *Fat4* and *Vangl2* (Extended Data Figs. 4a–e, 5b). Consistent with this, confocal immunofluorescence microscopy and transmission electron microscopy images showed the expression of tight-junction and gap-junction proteins, as well as the presence of definite tight junctions, adherens junctions, desmosomes and prominent cellular interdigitations at the cell–cell border of CX$_3$CR1$^+$ lining macrophages (Extended Data Figs. 6, 7a–d). The results of confocal immunofluorescence microscopy and flow cytometry of human synovial tissue confirmed a dense macrophage lining, consisting of closely associated TREM2$^+$ macrophages that also expressed tight-junction proteins (Extended Data Fig. 8a–c). These TREM2$^+$MHCII$^-$ macrophages comprised 10–30% of the total human synovial macrophages during steady state in samples derived from patients with osteoarthritis, but were seemingly outnumbered by TREM2$^-$ mononuclear phagocytes that dominated the disrupted synovial lining of patients with rheumatoid arthritis (Extended Data Fig. 8b–e).

Tight junctions between synovial lining macrophages rapidly disintegrated both during STA and during human rheumatoid arthritis, correlating with the changing physical density of this macrophage network during the onset and resolution of inflammation (Fig. 4a, b, Extended Data Figs. 6, 7e–i, 8a–e, 9a). Magnetic resonance imaging confirmed that this disintegration of the tight-junction-mediated barrier of macrophages was accompanied by an increased intra-articular influx of contrast agent during the initiation of STA (Fig. 4c, Extended Data

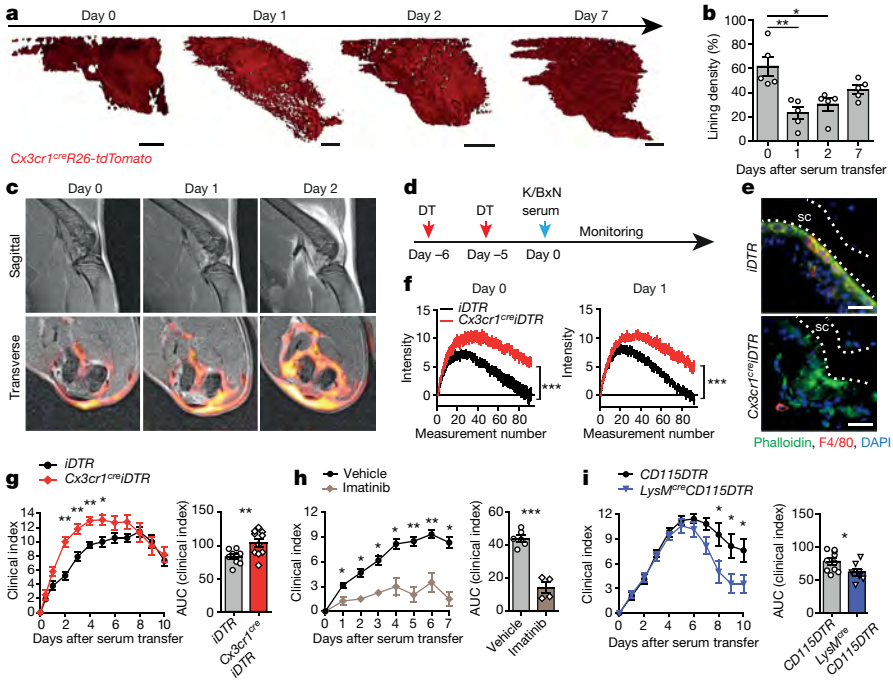

Fig. 4 | CX_3CR1^+ synovial lining macrophages provide a tight junction-mediated anti-inflammatory barrier for the joint. a, **b**, LSFM-derived 3D reconstruction of spatiotemporal changes (**a**) and calculated lining density (**b**) of tdTomato$^+$ macrophages from the knees of *Cx3cr1^{cre}R26-tdTomato* mice ($n = 5$) at the indicated days (0–7) after the induction of K/BxN STA. Data are mean ± s.e.m.; Kruskal–Wallis *H*-test with Dunn's multiple comparison test, $^{**}P = 0.0025$, $^{*}P = 0.034$. Scale bars, 100 μm. **c**, Representative magnetic resonance imaging analysis of knee joints at the indicated days ($n = 4$ each day) of STA showing sagittal T1-weighted images after the application of contrast agent (top) and transverse T1-weighted images after the application of contrast agent and merged with T1-weighted dynamic-contrast-enhanced colour maps (bottom). The merged magnetic resonance images include a colour-coded map of the area under the curve (AUC) of contrast-agent accumulation over 12 min (bottom), ranging from yellow (high AUC values) to red (low AUC values). **d**, Depletion strategy for CX_3CR1^+ lining macrophages. *Cx3cr1^{cre}iDTR* and *iDTR* control mice received 2 × 500 ng DT intraperitoneally 5 days before the administration of K/BxN serum. **e**, Representative bright-field fluorescence microscopy of the synovial lining on day 5 after the application of DT (phalloidin, green; F4/80, red; DAPI, blue). **f**, Normalized signal intensity curves from the dynamic-contrast-enhanced magnetic resonance imaging of synovial tissue from the knee joints of DT-treated mice at the indicated days of STA, over 90 measurements with intervals of 7 s in *Cx3cr1^{cre}iDTR* ($n = 8$ knee joints) and *iDTR* control mice ($n = 10$ knee joints). Data are mean ± s.e.m. of AUC, two-tailed Student's *t*-test; day 0, $^{***}P = 0.0003$; day 1, $^{***}P = 0.0001$. **g**, Clinical course of STA, including AUC of the corresponding clinical index, in *Cx3cr1^{cre}iDTR* ($n = 10$) and *iDTR* control ($n = 9$) of DT-treated mice. Data are mean ± s.e.m.; two-tailed Mann–Whitney *U*-test for clinical index with $^{*}P \leq 0.05$ and $^{**}P \leq 0.01$; two-tailed Student's *t*-test for AUC, $^{**}P = 0.0093$. **h**, Clinical course of STA, including AUC of the corresponding clinical index, in C57BL/6 wild-type mice treated with imatinib (80 μg kg^{-1}, oral gavage, twice daily, $n = 4$) or vehicle ($n = 6$) starting one day before the induction of STA. Mean ± s.e.m.; Mann–Whitney *U*-test for clinical index with $^{*}P \leq 0.05$ and $^{**}P \leq 0.01$; two-tailed Student's *t*-test for AUC with $^{***}P = 0.0001$. **i**, Clinical course of STA, including AUC of the corresponding clinical index, in *LysM^{cre}CD115DTR* ($n = 7$) and *CD115DTR* control mice ($n = 10$) treated with DT (500 ng per mouse intraperitoneally) starting one day before STA induction followed by a daily intraperitoneal injection of 100 ng DT. Mean ± s.e.m.; Mann–Whitney *U*-test for clinical index with $^{*}P \leq 0.05$; two-tailed Student's *t*-test for AUC, $^{*}P = 0.0417$.

Fig. 9b). This inflammation-associated barrier breakdown occurred after the deposition of autoantibody-containing immune complexes, which were immediately ingested by CX_3CR1^+ lining macrophages (Extended Data Fig. 9c, d). Depletion of PMNs and Ly6C^{high} inflammatory monocytes did not interfere with barrier breakdown, indicating that disintegration of tight junctions within the synovial macrophage lining resulted from an initial immune-complex-mediated activation of CX_3CR1^+ lining macrophages and was independent of the recruitment of inflammatory myeloid cells (Extended Data Fig. 9e, f). To investigate the role of tight-junction-expressing CX_3CR1^+ macrophages during arthritis, we crossed *Cx3cr1^{cre}* mice with mice containing a Cre-inducible DT receptor (*Cx3cr1^{cre}R26-iDTR* mice), allowing for the DT-mediated depletion of CX_3CR1^+ resident synovial lining macrophages. This protocol resulted in the additional depletion of a proportion of blood monocytes; however, with the exception of tissue-resident macrophages, they repopulated within 48 h (Fig. 4d, e, Extended Data Fig. 9g). Magnetic resonance imaging on day 5 after DT injection confirmed that the selective absence of CX_3CR1^+ macrophages indeed abolished the synovial barrier in healthy mice, which corresponded to the barrier breakdown observed during the onset of arthritis (Fig. 4f). Both systemic and local depletion of CX_3CR1^+ lining macrophages—as well as forced disintegration of tight junctions upon the injection of claudin 5 peptidomimetics—resulted in a disrupted barrier function, an early and exacerbated onset of arthritis and accelerated PMN influx (Fig. 4g, Extended Data Fig. 9h–k). Together, these data suggest that this subset of macrophages exerts an important immune-regulatory function by maintaining a physical and functional tight-junction-mediated barrier that secludes and protects intra-articular structures and thereby controls the onset of inflammation. Consistent with this, the tyrosine kinase inhibitor imatinib—which has been shown to stabilize the formation of tight junctions at the blood–brain barrier[18]—was found to interfere with the onset of arthritis (Fig. 4h). During STA in *Lysm^{cre}CD115DTR* mice, DT-mediated depletion of CSF1R$^+$ monocytes and macrophages occurred without directly targeting CSF1R$^-$$CX_3CR1^+$ lining macrophages—an intervention that did not affect the onset of arthritis but, in accordance with a pro-inflammatory role of monocyte-derived macrophages, accelerated the resolution of inflammation (Fig. 4i, Extended Data Fig. 9l).

Our data reveal a complex functional specialization within synovial macrophage subsets and demonstrate the divergent roles of different tissue-resident and monocyte-derived macrophages during homeostasis and inflammation. The identification of an internal, locally

renewing and protective tight-junction-mediated macrophage barrier has important implications for our general understanding of the role of macrophages in health and disease (Extended Data Fig. 10). Other tissue-resident macrophages might use similar mechanisms to fulfil related gatekeeping functions, thereby determining the onset and resolution of inflammation, modulating host defence[19], preventing neutrophil-driven inflammatory tissue damage[20] or potentially interfering with an anti-tumour immune response.

Online content

Any methods, additional references, Nature Research reporting summaries, source data, extended data, supplementary information, acknowledgements, peer review information; details of author contributions and competing interests; and statements of data and code availability are available at https://doi.org/10.1038/s41586-019-1471-1.

Received: 4 October 2018; Accepted: 5 July 2019;
Published online 7 August 2019.

1. Udalova, I. A., Mantovani, A. & Feldmann, M. Macrophage heterogeneity in the context of rheumatoid arthritis. *Nat. Rev. Rheumatol.* **12**, 472–485 (2016).
2. Firestein, G. S. & McInnes, I. B. Immunopathogenesis of rheumatoid arthritis. *Immunity* **46**, 183–196 (2017).
3. Orr, C. et al. Synovial tissue research: a state-of-the-art review. *Nat. Rev. Rheumatol.* **13**, 463–475 (2017).
4. Croft, A. P. et al. Distinct fibroblast subsets drive inflammation and damage in arthritis. *Nature* **570**, 246–251 (2019).
5. Barrera, P. et al. Synovial macrophage depletion with clodronate-containing liposomes in rheumatoid arthritis. *Arthritis Rheum.* **43**, 1951–1959 (2000).
6. Haringman, J. J. et al. Synovial tissue macrophages: a sensitive biomarker for response to treatment in patients with rheumatoid arthritis. *Ann. Rheum. Dis.* **64**, 834–838 (2005).
7. Misharin, A. V. et al. Nonclassical Ly6C$^-$ monocytes drive the development of inflammatory arthritis in mice. *Cell Rep.* **9**, 591–604 (2014).
8. Zhang, F. et al. Defining inflammatory cell states in rheumatoid arthritis joint synovial tissues by integrating single-cell transcriptomics and mass cytometry. *Nat. Immunol.* **20**, 928–942 (2019).
9. Ginhoux, F. et al. Fate mapping analysis reveals that adult microglia derive from primitive macrophages. *Science* **330**, 841–845 (2010).
10. Schulz, C. et al. A lineage of myeloid cells independent of Myb and hematopoietic stem cells. *Science* **336**, 86–90 (2012).
11. Yona, S. et al. Fate mapping reveals origins and dynamics of monocytes and tissue macrophages under homeostasis. *Immunity* **38**, 79–91 2013).
12. Hashimoto, D. et al. Tissue-resident macrophages self-maintain locally throughout adult life with minimal contribution from circulating monocytes. *Immunity* **38**, 792–804 (2013).
13. Rosas, M. et al. The transcription factor Gata6 links tissue macrophage phenotype and proliferative renewal. *Science* **344**, 645–648 (2014).
14. Okabe, Y. & Medzhitov, R. Tissue-specific signals control reversible program of localization and functional polarization of macrophages. *Cell* **157**, 832–844 (2014).
15. Lavin, Y. et al. Tissue-resident macrophage enhancer landscapes are shaped by the local microenvironment. *Cell* **159**, 1312–1326 (2014).
16. Chakarov, S. et al. Two distinct interstitial macrophage populations coexist across tissues in specific subtissular niches. *Science* **363**, eaau0964 (2019).
17. Aziz, A., Soucie, E., Sarrazin, S. & Sieweke, M. H. MafB/c-Maf deficiency enables self-renewal of differentiated functional macrophages. *Science* **326**, 867–871 (2009).
18. Armulik, A. et al. Pericytes regulate the blood–brain barrier. *Nature* **468**, 557–561 (2010).
19. Cronan, M. R. et al. Macrophage epithelial reprogramming underlies mycobacterial granuloma formation and promotes infection. *Immunity* **45**, 861–876 (2016).
20. Uderhardt, S., Martins, A. J., Tsang, J. S., Lämmermann, T. & Germain, R. N. Resident macrophages cloak tissue microlesions to prevent neutrophil-driven inflammatory damage. *Cell* **177**, 541–555.e17 (2019).

METHODS

For additional information on materials used, see Supplementary Table 3.

Ethical compliance. We complied with all relevant ethical regulations in terms of animal experiments and human samples in this study. All animal experiments conducted at the University of Erlangen were performed in accordance with German guidelines and laws, were approved by local animal ethic committees of the Regierung von Mittelfranken and were conducted according to the guidelines of the Federation of European Laboratory Animal Science Associations. Parabiosis experiments were approved by the Animal Care and Ethics Committee of the Centro Nacional de Investigaciones Cardiovasculares and local authorities.

Synovial biopsies were obtained from knee joints of patients diagnosed with osteoarthritis or rheumatoid arthritis. Patients with rheumatoid arthritis fulfilled the 2010 EULAR/ACR criteria of rheumatoid arthritis. All patients were ≥18 years of age. Patients with osteoarthritis were recruited at the Department of Trauma Surgery, University Hospital Erlangen and patients with rheumatoid arthritis were recruited at the Department of Internal Medicine 3 - Rheumatology and Immunology, University Hospital Erlangen. All patients signed an informed consent form, which was approved by the local ethics committee of the University Hospital Erlangen.

Mice. For all experiments, mice of both sexes were used. For details regarding mouse strains, see Supplementary Table 3. All mice used were aged between 8 and 18 weeks, unless stated otherwise. No statistical methods were used to predetermine sample size.

To generate *Cx3cr1^{cre}R26-tdTomato* mice, STOCK Tg(Cx3cr1^{cre})MW126Gsat/Mmucd mice (identification number 036395-UCD) were obtained from the Mutant Mouse Regional Resource Center (MMRC), a National Institutes of Health (NIH)-funded strain repository, and were donated to the MMRRC by the National Institute of Neurological Disorders and Stroke (NINDS)-funded GENSAT BAC transgenic project. B6.129P2(C)-*Cx3cr1$^{tm2.1(cre/ERT2)Jung}$*/J (*Cx3cr1^{ERcre}*), FVB-Tg(Csf1r-cre/Esr1*)1Jwp/J (*CSF1R^{ERcre}*), C57BL/6-Gt(ROSA)26Sortm1(HBEGF)Awai/J (*iDTR*), B6;129S6-*Gt(ROSA)26Sor$^{tm9(CAG-tdTomato)Hze}$*/J (*tdTomato*), C57BL/6-Tg(Csf1r-HBEGF/mCherry)1Mnz/J (*CD115DTR*) and B6.129P-Cx3cr1tm1Litt/J (*Cx3cr1^{GFP}*) mice were purchased from Jackson Laboratories. These mice were bred and housed at the animal facilities of the University of Erlangen under specific-pathogen-free conditions. *ColVI^{cre}* mice were generated in the laboratory of G. Kollias and have previously been described[21]. *Retnla^{cre}R26-tdTomato* mice were generated in the laboratory of D. Vöhringer[22].

In vivo treatments and arthritis induction. K/BxN STA was induced by the injection of K/BxN serum collected from arthritic K/BxN mice. Clinical development of arthritis was evaluated using a clinical index ranging from 0 (minimum) to 16 (maximum), which represents a cumulative score of 0 to 4 for each paw, with 0 = no signs of inflammation; 1 = minor swelling and reddening of a paw, or affecting only single digits; 2 = moderate swelling and erythema, or affecting multiple digits per paw; 3 = severe swelling and erythema affecting the whole paw; 4 = maximum swelling and erythema. Measurements of hind-paw swelling were conducted using dial thickness gauges (Peacock).

Cx3cr1^{creER}tdTomato mice were treated systemically with 4 mg tamoxifen dissolved in peanut oil intraperitoneally (i.p.) twice within 48 h. *Csf1r^{creER}R26-tdTomato* mice were fed with tamoxifen-containing food (400 mg kg^{-1} tamoxifen citrate, Envigo) for 5 days, 4 weeks or 6 weeks. Local administration of (*Z*)-4-hydroxytamoxifen (Sigma-Aldrich, H7904) was performed by intra-articular injection of 25 µl of (*Z*)-4-hydroxytamoxifen (2 mM) dissolved in PBS/4% ethanol into the right knee joint. Five days after injection, K/BxN serum transfer arthritis was induced. Mice were analysed seven days after the induction of arthritis.

For systemic administration of DT, *Cx3cr1^{cre}iDTR* mice received 500 ng DT per mouse i.p. on 2 consecutive days, beginning 6 days before the induction of STA. Local depletion of macrophages in *Cx3cr1^{cre}iDTR* mice was induced by the injection of 50 ng DT in 50 µl PBS directly into the hind paw 3 days before the induction of STA. The contralateral hind paw was injected with PBS and served as a control.

LysM^{cre}CD115DTR mice received a single dose of 500 ng DT per mouse (i.p.) 1 day before the induction of arthritis followed by daily injections of 100 ng DT per mouse (i.p.). To study the depletion of synovial macrophages in *LysM^{cre}CD115DTR* mice under healthy conditions, 500 ng DT per mouse was injected intraperitoneally 3 times a week until day 10.

The claudin peptidomimetics[23] (C5C2, sequence SSVVQSTGHMQSKV YESVLALSAEVQAAR-NH2) and scrambled variant (C5C2scr, AHLVRSVSD VMQSQTGKTSESYSAVQLVA-NH2) were dissolved in PBS and injected intravenously (i.v.) (3.5 µmol kg^{-1}) one day before and one day after the induction of STA for clinical evaluation, with a single injection one day before the induction of STA for the magnetic resonance imaging experiments.

Imatinib (80 µg kg^{-1}) was given orally twice a day, starting one day before the induction of STA. Imatinib was dissolved in aqueous vehicle solution containing 0.5% (hydroxypropyl)cellulose and 0.05% TWEEN 80.

K/BxN serum IgG was isolated with protein-G Gravi-Trap (GE Healthcare, 28-9852-55) and labelled using SAIVI Alexa Fluor 647 Antibody/Protein 1 mg-Labelling Kit. Labelled IgGs were injected i.v. with K/BxN serum at a ratio of 1:4.

Collagen-induced arthritis was induced as previously described[24]. In brief, C67BL/6 mice were immunized by intradermal injection of an emulsion of 200 µg of chicken type II collagen (Sigma-Aldrich, C-930) with 250 µg heat-inactivated *Mycobacterium tuberculosis* H37RA in incomplete Freund's adjuvant (Sigma-Aldrich, F5506) at day 0 and day 21.

Depletion of neutrophils and Ly6C$^+$ monocytes was performed by i.v. injection of 200 µg InVivoPlus anti-mouse Ly6G/Ly6C (Gr-1) (clone: RB6-8C5, Bio X Cell, BP0075) one day before K/BxN serum transfer. InVivoPlus rat IgG2b isotype control, anti-keyhole limpet haemocyanin (200 µg, i.v., clone: LTF-2, Bio X Cell, BP0090) served as control.

The severity of both K/BxN STA and collagen-induced arthritis was scored in a blinded manner. Mice were not randomized before the experiment.

Parabiosis. Parabiosis was performed following a previously described procedure[25]. Mice were shaved under anaesthesia at the corresponding lateral region and incisions were made from the olecranon to the knee joint of each mouse. Olecranons and knee joints of partner mice were tied together by a single 5-0 polypropylene suture. Dorsal and ventral skins were stitched up forming a continuous suture. Finally, each mouse received a single injection of buprenorphine subcutaneously. Analysis was performed as indicated six or nine weeks after surgery. The tissue chimerism was calculated as the quotient of the ratios of partner-derived macrophages of synovial joints and the ratio of partner-derived monocytes in the blood as quantified by flow cytometry. A tissue-to-blood chimerism of one thus represents an equal ratio between blood and tissue.

Flow cytometry and fluorescence-activated cell sorting. For isolation of synovial macrophages, hind paws were dissected by removing skin, muscle and tendons. Cells were dissociated by incubation for 45 min in a digestion medium consisting of RPMI medium, 10% heat-inactivated fetal calf serum (FCS), collagenase (2 mg ml^{-1}) from *Clostridium histolyticum* (Sigma-Aldrich, C5138-1G) and 0.03 mg ml^{-1} DNase (Sigma-Aldrich, 9003-98-9). After washing with PBS containing 2% heat-inactivated FCS and 2 mM EDTA, cells were blocked with 10% rat serum in PBS for 10 min at room temperature and stained with fluorophore-conjugated antibodies for 20 min at 4 °C. After washing with PBS, cells were resuspended in FACS buffer (PBS, 2% FCS). EdU, which was injected intraperitoneally (50 mg kg^{-1}) 4 h before collecting the cells, was detected using the EdU base click EdU-Flow Cytometry Kit 488 (BCK-FC488-100).

Human synovial tissue was dissociated in digestion medium containing RPMI medium, 10% heat-inactivated fetal calf serum (FCS), collagenase (2 mg ml^{-1}) from *C. histolyticum* (Sigma, C5138-1G) and 0.03 mg ml^{-1} DNase (Sigma, 9003-98-9) at 37 °C for 45 min. After washing with PBS, cells were incubated with Zombie Aqua (1:1,000, BioLegend) for 15 min at room temperature. Dissociated cells were fixed with 4% PFA/PBS, incubating for 15 min at room temperature. After washing with 1% BSA/PBS, cells were resuspended in saponin-based permeabilization buffer containing the following antibodies: CD11b-AF488, MHC II-PE, CD14-PeCy7, CD45-AF700, CD1c-PerCP/Cy5.5, CD20-BV421, CD15-BV421 and TREM2-APC, overnight at 4–8 °C.

Flow cytometry was performed with a CytoFLEX S, Beckman Coulter. Sorting of cells was performed with a MoFlo XDP, Beckman Coulter and the Summit Software System. Data were analysed with Kaluza (Beckman Coulter, v.1.5a), CytExpert (Beckman Coulter, v.2.2.0.97) or FlowJo (v.7.6.5).

Bulk RNA sequencing of sorted CX_3CR1^+ and CX_3CR1^- macrophages and bone-marrow-derived macrophages. Tissues from *Cx3cr1^{GFP}* mice were prepared for sorting of synovial macrophages as described in the section 'Flow cytometry and fluorescence-activated cell sorting'. Macrophages were defined as CD45$^+$CD11b$^+$F4/80$^+$. Expression of enhanced GFP discriminated CX_3CR1^+ lining and CX_3CR1^- macrophages. For generating BMDMs, bone marrow cells were isolated from femurs of C57BL/6 mice and cultured for one day in DMEM (10% FCS, 1% penicillin–streptomycin). Non-adherent macrophage precursors were cultivated and differentiated to macrophages for 5 days in M-CSF-conditioned DMEM medium (10% FCS, 1% penicillin–streptomycin). Isolation of RNA was performed using the RNeasy Mini kit (Qiagen, 74104). Libraries were subjected to single-end sequencing (101 bp) on a HiSeq-2500 platform (Illumina). The obtained reads were converted to .fastq format and demultiplexed using bcl2fastq v2.17.1.14. Quality filtering was performed using cutadapt v. 1.15; then reads were mapped against the mouse reference genome (Ensembl GRCm38, release 91) using the STAR aligner v.2.5.4a[26], and a STAR genome directory created by supplying the Ensembl gtf annotation file (release 91). Read counts per gene were obtained using featureCounts program v.1.6.1[27] and the Ensembl gtf annotation file. The subsequent analyses were performed using R v.3.5.0. In particular, differential expression analysis was performed with the DESeq2 package v.1.20.0[28] and plots were generated with the ggplot2_2.2.1 package.

Quantitative real-time PCR of sorted CX_3CR1^+ macrophages and BMDMs. RNA of sorted GFP^+ macrophages from *Cx3cr1*^{GFP} mice and BMDMs was isolated using the RNeasy Mini kit (Qiagen, 74104). Reverse transcription of total RNA was performed with human leukaemia virus reverse transcriptase using the Gene Amp RNA PCR kit (Applied Biosystems) and oligo$(dT)_{16}$ primers (Invitrogen). Quantification of gene expression was performed as previously described[29]. The following primer sequences were used: β-actin: TGT CCA CCT TCC AGC AGA TGT (sense), AGC TCA GTA ACA GTC CGC CTA GA (antisense); ZO-1: GCT AAG AGC ACA GCA ATG GA (sense), GCA TGT TCA ACG TTA TCC AT (antisense); claudin 5: TTA AGG CAC GGG TAG CAC TCA CG (sense), TTA AGG CAC GGG TAG CAC TCA CG (antisense), claudin 10: TGG TGT GTG GTG TTG GAG GGT TTG G (sense), TGG AAG GAG CCC AGA GCG TTA CCT G (antisense)[30,31].

Single-cell sequencing of sorted myeloid cells of different stages of arthritis. Sorted $CD45^+CD11b^+Ly6G^-$ synovial cells of hind paws of mice at steady state (day 0) and at different stages of K/BxN STA (day 1, day 2 and day 5 after serum transfer) were subjected to 10x Chromium Single Cell 3′ Solution v2 library preparation according to the manufacturer's instructions. Library sequencing was performed on an Illumina HiSeq 2500 sequencer to a depth of 100 million reads each. Reads were converted to .fastq format using mkfastq from cellranger 2.1.0 (10x Genomics). Reads were then aligned to the mouse reference genome (mm10, Ensembl annotation release 91) including the additional sequence and feature annotation for tdTomato. Alignment was performed using the count command from cellranger 2.1.0 (10x Genomics). Primary analysis, quality control filtering (gene count per cell, unique molecular identifier count per cell, percentage of mitochondrial transcripts), clustering, cell-cycle phase scoring based on canonical markers and regression, identification of cluster markers and visualization of gene expression were performed using the Seurat (v.2.3)[32] package for R.

Construction of single-cell trajectories, identification of genes changing as a function of pseudotime and clustering of genes by pseudotemporal expression patterns were performed using the Monocle 2 package for R. Pseudotime calculations were performed on the top 1,000 differentially expressed genes between clusters[33,34]. For gene ontology enrichment analysis of biological processes, the PANTHER Statistical Overrepresentation Test (http://www.pantherdb.org) was used.

Cryo-sectioning of mouse knee joints. Mouse long bones were fixed in 4% PFA/PBS (pH 7.4) for 12 h at 4–8 °C, incubated for 10 days in decalcification buffer (14% EDTA free acid, NH_4OH, pH 7.2) and embedded in OCT Compound (Sakura Finetek). A Leica CM 3050 S cryostat and Cryofilm Type 2C(9) (C-MK001-A2, Section-Laboratory) were used for the generation of 7-μm-thick histological sections.

Histological immunofluorescence staining. For staining cryo-sections of mouse knee joints, samples were blocked with rat serum or 0.2% BSA and permeabilized with 0.1% saponin in PBS for 1 h at room temperature. For immunofluorescence staining, the antibodies listed in Supplementary Table 3 were used. Staining was performed for 4 h at room temperature or overnight at 4 °C using the indicated antibodies diluted in blocking solution. Unbound primary antibodies were washed off with DPBS and unlabelled primary antibodies were counterstained with donkey anti-Rabbit IgG AF488 or AF647 antibody in blocking solution for 4 h at room temperature and washed with DPBS. Joint sections were stained with DAPI or SYTOX Blue by incubating samples for 10 min (DAPI) or 1 h (SYTOX Blue) at room temperature. Samples were washed three times with DPBS, once with water for injection, and embedded onto a coverslip with Dako Fluorescence Mounting Medium.

Bright-field fluorescence microscopy of histological samples. Histological joint samples were imaged with an upright Nikon Eclipse Ni-U microscope, using a 10× (numerical aperture (NA) 0.30), 20× (NA 0.50) or 40× (NA 0.75) CFI Plan Fluor objective for varying magnifications. The halogen lamp excitation light (of wavelength λ_{ex}) as well as the emitted light (λ_{em}) was filtered specifically according to individual excitation/emission profiles: DAPI λ_{ex}: 390/18 nm and λ_{em}: 460/60 nm, fluorescein isothiocyanate (FITC)/AF488 λ_{ex}: 475/35 nm and λ_{em}: 530/43 nm, tdTomato/AF594 λ_{ex}: 542/20 nm and λ_{em}: 620/52 nm, AF647 λ_{ex}: 628/40 nm and λ_{em}: 692/40 nm. The generated data were processed with Imaris software.

Confocal laser scanning microscopy of histological samples. For high-magnification imaging of histological joint sections, a Leica TCS SP 5 II confocal microscope with acousto-optic tunable filter and acousto-optical beam splitter, and hybrid detector (HyD) on a DMI6000 CS frame was used. Imaging of coverslip-embedded samples was performed using an HCX PL APO 100× oil objective with a NA of 1.44. Fluorescence signals were generated via sequential scans, exciting tdTomato using a diode-pumped solid-state laser at 561 nm and detecting with a HyD at 600–650 nm. The second sequence for visualizing Alexa Fluor 488 or FITC-labelled staining included an argon laser at 488 nm for excitation and a HyD detector at 500–550 nm. A third imaging sequence involved a simultaneous excitation of SYTOX Blue with a 458-nm argon laser and of Alexa Fluor 647 staining with a 633-nm helium-neon laser. SYTOX Blue was detected by HyD at 470–520 nm and Alexa Fluor signals were detected by HyD at 650–700 nm. Generated images were deconvoluted with Huygens Professional and 3D-reconstructed with Imaris software.

Spinning disk confocal microscopy of histological samples. For spinning disk confocal microscopy of histological joint sections, an inverted Zeiss Spinning Disc Axio Observer.Z1 with a Yokogawa CSU-X1M 5000 spinning disk unit, a LD C-Apochromat 63× water immersion objective (NA 1.15) and an Evolve 512 EMCCD camera was used. Fluorescence signals were excited and detected as follows: DAPI λ_{ex}: 405 nm DPSS laser and λ_{em}: 445/50 nm BP filter, AF488 λ_{ex}: 488 nm DPSS laser and λ_{em}: 525/50 nm BP filter, tdTomato λ_{ex}: 561 nm DPSS laser and λ_{em}: 605/70 nm BP filter. Acquired images were processed via Zen Blue 2.3 image acquisition software.

Optical clearing of mouse joint samples. Optically cleared samples for light-sheet fluorescence microscopy were generated as previously described[35]. In detail, mice received 2.5 μg Ly6G-AF647 or CD31-AF647 in PBS i.v. and were euthanized after 1 h. Mice were perfused with 5 mM EDTA/PBS and perfusion-fixed with 4% PFA/PBS (pH 7.4). Knee joints were relieved from muscle tissue and post-fixed in 4% PFA/PBS (pH 7.4) for 4 h at 4–8 °C with gentle shaking. Tissue fixation was followed by dehydration. Tissue dehydration was performed by increasing the proportion of ethanol according to the following series: 50%, 70% and two consecutive incubations with 100% ethanol each. The 50% and 70% ethanol solutions were generated by diluting 100% ethanol with water for injection, and their pH values were adjusted to 9.0 using NaOH. All tissue dehydration steps were performed at 4–8 °C in gently shaking 5 ml tubes. After tissue dehydration, joint samples were transferred to ethyl cinnamate and incubated at room temperature for 6 h.

LSFM of optically cleared samples. LSFM of optically cleared mouse knee joints was performed with a LaVison BioTec Ultramicroscope II including an Olympus MVX10 zoom body (Olympus), a LaVision BioTec Laser Module, and an Andor Neo sCMOS Camera with a pixel size of 6.5 μm. Detection optics with an optical magnification range from 1.263 to 12.63 and a NA of 0.5 were used.

For visualization of general tissue morphology, a 488-nm optically pumped semiconductor laser (OPSL) was used to generate autofluorescent signals. For tdTomato excitation, a 561-nm OPSL and for CD31-AF647 or Ly6G-AF647 excitation, a 647-nm diode laser was used. Emitted wavelengths were detected with specific detection filters: 525/50 nm for autofluorescence, 620/60 nm for tdTomato, and 680/30 nm for CD31-AF647 or Ly6G-AF647. The optical zoom factor of the measurements varied from 1.26 to 8 and the light-sheet thickness ranged from 5 to 10 μm.

Three-dimensional lining density analysis. The density of the synovial lining was analysed by a volumetric ratio of $tdTomato^+$ lining macrophages to synovial tissue.

Three-dimensional reconstruction of LSFM-scanned mouse knee joints was performed using Imaris software. The synovial lining was optically separated from the joint tissue by manual surface rendering. Volumes of the isolated synovial lining tissue and $tdTomato^+$ lining cells were fully automatically rendered by the Imaris volume rendering tool with a size threshold of 5 μm for $tdTomato^+$ cells and 10 μm for synovial tissue. The percentage lining density was calculated from the ratio of cell and tissue volumes.

Magnetic resonance imaging. Magnetic resonance imaging (MRI) data were acquired using the ClinScan 70/30 7 T MRI System (Bruker) and a RatBrain 1H-Surface Coil (Bruker). Before measurement, mice were anaesthetized and a tail-vein catheter was placed for the injection of contrast agent during measurement. The body temperature was kept constant with a heating blanket and the respiration rate was monitored constantly. Anaesthesia was maintained with isoflurane. Dynamic contrast-enhanced (DCE) MRI was conducted using a fast low angle shot (FLASH) sequence with repetition time (TR)/echo time (TE): 2.92 ms/0.88 ms, flip angle: 25°, voxel size: 0.182 × 0.182 × 0.7 mm, matrix 192 × 192, acquisition time of 12 min and 100 measurements. The contrast agent (0.1 mmol kg^{-1} Gadovist, Bayer) was injected after 40 s over a time period of 10 s. Sagittal and transverse T1-weighted images were acquired after running the DCE sequence with the following specifications: voxel size: 0.078 × 0.078 × 0.7 mm, TR/TE: 500 ms/9 ms, matrix 448 × 448. The mean contrast agent enrichment over time in the synovial tissue set as region of interest was analysed using Horos software (https://horosproject.org/).

Transmission electron microscopy. Mouse knee joints were fixed in ITO fixation solution containing 2.5% glutaraldehyde (Roth, 4157.1), 2.5% paraformaldehyde (Roth, 0335.3), 0.1 M cacodylate buffer (Roth, 5169.2) and 0.3% picric acid dissolved in phosphate-buffered saline (pH 7.3) for two days, decalcified in cacodylate buffer (0.1 M) containing 14% EDTA for two weeks and finally embedded in Epon. Ultra-thin sections (Microtome, Reichert Ultracut S) of 50 nm were contrasted with uranyl acetate and lead(ii) acetate trihydrate and finally imaged with a transmission electron microscope (JEM 1400 Plus, Jeol).

Statistics and reproducibility. For calculations of statistical significance, GraphPad Prism 5 was used. Data are presented as mean ± s.e.m. and were analysed using the two-sided Student's *t*-test, the Mann–Whitney *U*-test or the Kruskal–Wallis *H*-test with Dunn's multiple comparisons test as post hoc procedure unless stated otherwise. *P* values less than 0.05 were considered significant. LSFM of Fig. 1a is representative of ten individual mice. Experiments in Fig. 1b, c were performed three times. Bright-field microscopy (BFM), CLSM and LSFM images of Fig. 1d and Extended Data Fig. 1c–e are representative images of three experiments with three mice each per day. Extended Data Fig. 1a, f are representative images of three individual mice. Flow cytometry experiments in Extended Data Fig. 1a were performed three times. Images in Extended Data Fig. 1g, h are representative of at least three individual mice. Parabiosis experiments and analysis of Fig. 2a, e, f and Extended Data Fig. 2d–k were performed once each per parabiotic combination and time points and images were representative of at least three mice. Images in Fig. 2b and Extended Data Fig. 2b, c are representative of three individual mice. Images in Extended Data Fig. 2a are representative of three individual mice. Flow cytometry experiments in Fig. 2h, j and Extended Data Fig. 3f–h were performed once. Images in Fig. 2i and Extended Data Fig. 3e are representative of three mice per group. Experiments in Extended Data Fig. 3a–c were performed twice. Experiments in Extended Data Fig. 3e are representative of three individual mice per day. Bulk RNA-seq analysis of Fig. 3a, b and Extended Data Fig. 4a–c was performed once. RNA quantification experiments in Extended Data Fig. 4d using the sorting strategy in Extended Data Fig. 4a was performed once. Single-cell RNA profiling experiments of sorted cells of Fig. 3c, d and Extended Data Figs. 4f–j, 5a–c comprise four different datasets of four individual mice at steady state, day 1, day 2 and day 5 after K/BxN serum transfer. Images in Extended Data Fig. 4k are representative of three individual mice of experiments that are shown in Extended Data Fig. 4l, m that were performed once. Images in Extended Data Fig. 4n are representative of two individual mice. The experiments in Extended Data Fig. 4o, p were performed once and show representative images of one mouse per group and the corresponding statistics for each mouse. Extended Data Fig. 6 shows representative images of four individual mice. Images in Extended Data Fig. 7a are representative of four individual mice. Transmission electron micrographs in Extended Data Fig. 7 are representative of three mice per time point. CLSM images in Extended Data Fig. 8a are representative of six mice per time point. CLSM of Extended Data Fig. 8b, c and the corresponding lining density analysis are representative of two patients with osteoarthritis and three patients with rheumatoid arthritis. Flow cytometry analyses are representative of three patients with osteoarthritis and two patients with rheumatoid arthritis. Experiments in Fig. 4a, b and Extended Data Fig. 9a were performed twice. MRI experiments of Fig. 4c, f and Extended Data Fig. 9k were performed once. BFM images of Fig. 4e are representative of 3 mice per group. Mouse experiments of Fig. 4g and Extended Data Fig. 9j were performed twice. Mouse experiments of Fig. 4h, i and Extended Data Fig. 9i were performed once. Images in Extended Data Fig. 9c, d are representative of three individual mice per time point. Images in Extended Data Fig. 9h are representative of three individual mice per group. Flow cytometry experiments in Extended Data Fig. 9g, l were performed once and confirmed the depletion efficiency. Experiments shown in Supplementary Videos 1, 3 and 4 were performed three times, that in Supplementary Video 2 was performed once, and those in Supplementary Videos 5, 6 and 7 were each performed five times.

Reporting summary. Further information on research design is available in the Nature Research Reporting Summary linked to this paper.

Data availability

The data that support the plots within this paper and other findings of this study are available from the corresponding author upon request. The bulk and single-cell RNA-seq data are available as part of the Gene Expression Omnibus (GEO) SuperSeries GSE134691.

21. Armaka, M. et al. Mesenchymal cell targeting by TNF as a common pathogenic principle in chronic inflammatory joint and intestinal diseases. *J. Exp. Med.* **205**, 331–337 (2008).
22. Krljanac, B. et al. RELMα-expressing macrophages protect against fatal lung damage and reduce parasite burden during helminth infection. *Sci. Immunol.* **4**, eaau3814 (2019).
23. Dithmer, S. et al. Claudin peptidomimetics modulate tissue barriers for enhanced drug delivery. *Ann. NY Acad. Sci.* **1397**, 169–184 (2017).
24. Pfeifle, R. et al. Regulation of autoantibody activity by the IL-23–T_H17 axis determines the onset of autoimmune disease. *Nat. Immunol.* **18**, 104–113 (2017).
25. Casanova-Acebes, M. et al. Rhythmic modulation of the hematopoietic niche through neutrophil clearance. *Cell* **153**, 1025–1035 (2013).
26. Dobin, A. et al. STAR: ultrafast universal RNA-seq aligner. *Bioinformatics* **29**, 15–21 (2013).
27. Liao, Y., Smyth, G. K. & Shi, W. featureCounts: an efficient general purpose program for assigning sequence reads to genomic features. *Bioinformatics* **30**, 923–930 (2014).
28. Love, M. I., Huber, W. & Anders, S. Moderated estimation of fold change and dispersion for RNA-seq data with DESeq2. *Genome Biol.* **15**, 550 (2014).
29. Ipseiz, N. et al. The nuclear receptor Nr4a1 mediates anti-inflammatory effects of apoptotic cells. *J. Immunol.* **192**, 4852–4858 (2014).
30. Katsuno, T. et al. Deficiency of zonula occludens-1 causes embryonic lethal phenotype associated with defected yolk sac angiogenesis and apoptosis of embryonic cells. *Mol. Biol. Cell* **19**, 2465–2475 (2008).
31. Ohtsuki, S., Yamaguchi, H., Katsukura, Y., Asashima, T. & Terasaki, T. mRNA expression levels of tight junction protein genes in mouse brain capillary endothelial cells highly purified by magnetic cell sorting. *J. Neurochem.* **104**, 147–154 (2008).
32. Butler, A., Hoffman, P., Smibert, P., Papalexi, E. & Satija, R. Integrating single-cell transcriptomic data across different conditions, technologies, and species. *Nat. Biotechnol.* **36**, 411–420 (2018).
33. Trapnell, C. et al. The dynamics and regulators of cell fate decisions are revealed by pseudotemporal ordering of single cells. *Nat. Biotechnol.* **32**, 381–386 (2014).
34. Qiu, X. et al. Single-cell mRNA quantification and differential analysis with Census. *Nat. Methods* **14**, 309–315 (2017).
35. Klingberg, A. et al. Fully automated evaluation of total glomerular number and capillary tuft size in nephritic kidneys using lightsheet microscopy. *J. Am. Soc. Nephrol.* **28**, 452–459 (2017).

Acknowledgements We thank C. Stoll, A. Klej, L. Seyler, R. Palmisano and the Optical Imaging Center Erlangen for technical assistance. M. Mroz and U. Appelt provided help during cell sorting and W. Baum and U. Baschant helped to generate K/BxN serum. This work was supported by the Deutsche Forschungsgemeinschaft (DFG – FG 2886 "PANDORA" - B01/A03 to G.K. and G.S., the CRC1181-A03/A01/A02/Z2 to G.K., G.S., D.V. and T.B. and the GK 1660 to G.K.), the Emerging Field Initiative (EFI) of the Friedrich-Alexander University Erlangen-Nürnberg (FAU) and the STAEDTLER Stiftung (EFI_Verbund_Med_05_MIRACLE to G.K. and T.B.), the Bundesministerium für Bildung und Forschung (BMBF) (METARTHROS to G.K. and G.S.) and the European Union (Horizon 2020 ERC-2014-StG 640087 - SOS to G.K and Horizon 2020 ERC-2018-SyG nanoSCOPE and RTCure to G.S.). J.Á.N.-Á. was supported by fellowship SVP-2014-068595 and A.H. by grant SAF2015-65607-R from Ministerio de Ciencia, Investigacion y Universidades (MCIU), and co-funding by Fondo Europeo de Desarrollo Regional (FEDER). The CNIC is supported by the MCIU and the Pro CNIC Foundation, and is a Severo Ochoa Center of Excellence (MCIU award SEV-2015-0505). *Col1*^{cre} mice were provided by G. Kollias.

Author contributions S.C. and A.G. designed the study, performed experiments, interpreted results and wrote the manuscript. J.Á.N.-Á. designed the study and experiments and interpreted data. D.W., K.F., J.A.Q., K.F.L., T.R., M.F., J.A.A. and R.P. performed experiments and collected and interpreted data. A.K., D.S., M.P., K.G. and N.R. provided expertise, patient material and input and wrote the manuscript. T.B. designed, performed and interpreted the MRI measurements. B.K. and D.V. were involved in the generation of *Retnla*^{cre} mice and provided input. P.K., M.E., A.B.E., F.F. and J.V. performed bioinformatics analysis and interpreted the data. E.K. and M.S. performed electron microscopy experiments and interpreted the results. R.F.H. and I.E.B. designed and tested the claudin peptidomimetics, designed experiments and wrote the manuscript. F.P., G.S., A.H. and G.K. designed the study and experiments and wrote the manuscript. All authors read and commented on the manuscript.

Competing interests The authors declare no competing interests.

Additional information

Supplementary information is available for this paper at https://doi.org/10.1038/s41586-019-1471-1.

Correspondence and requests for materials should be addressed to G.K.

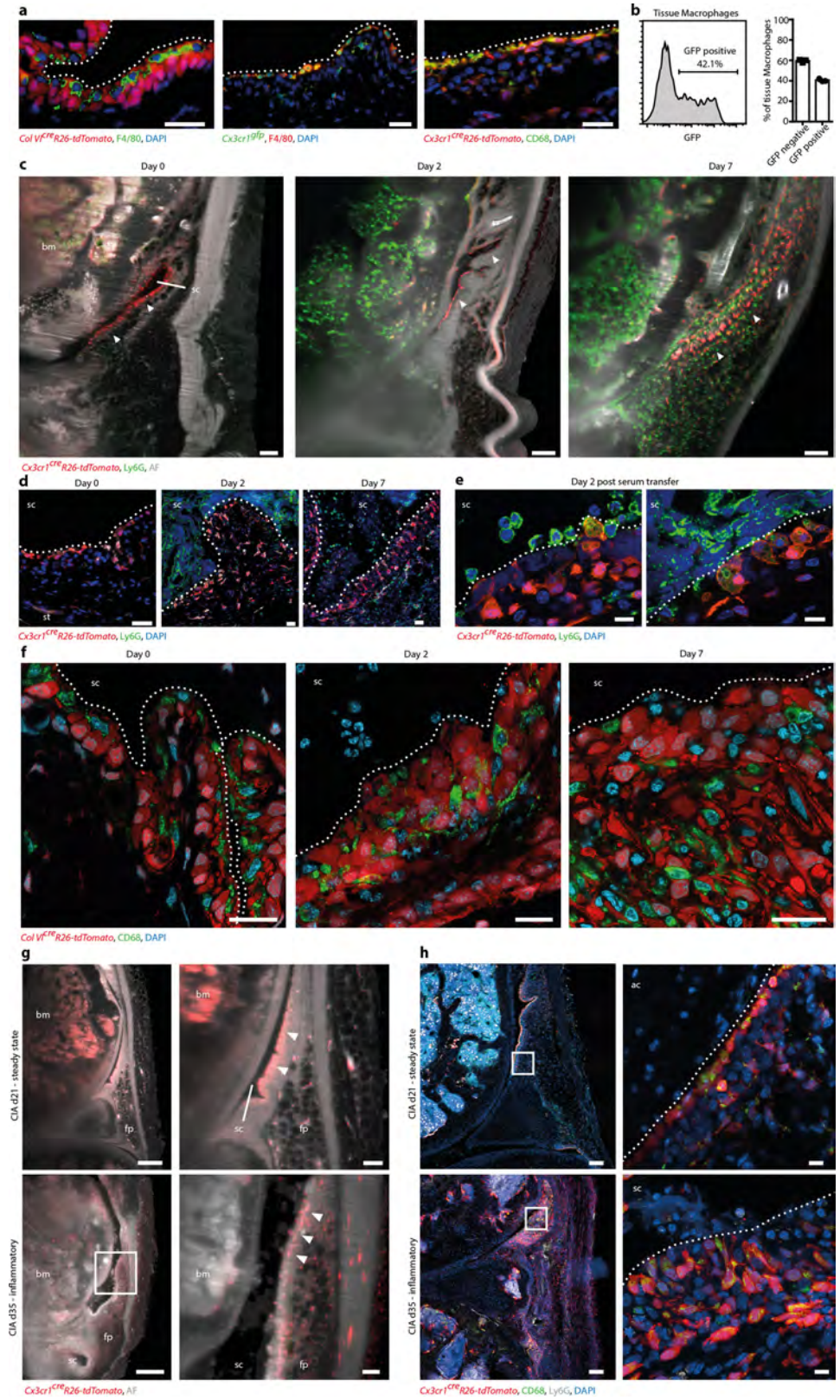

Extended Data Fig. 1 | See next page for caption.

Extended Data Fig. 1 | Spatiotemporal profiling of synovial CX_3CR1^+ macrophages. a, BFM of macrophages within the synovial tissue using the macrophage markers F4/80 (left and middle; colour as indicated) and CD68 (right; green) in *ColVI^{cre}R26-tdTomato* reporter mice (left; tdTomato$^+$, red), *Cx3cr1^{GFP}* mice (middle; GFP$^+$, green), and *Cx3cr1^{cre}R26-tdTomato*, mice (right; tdTomato$^+$, red). Scale bars, 25 μm. **b**, Flow cytometry analysis of macrophages of dissociated hind-paw joints of *Cx3cr1^{gfp}* mice ($n = 3$) gated for CD45$^+$, CD11b$^+$, F4/80$^+$ and GFP. Data are mean ± s.e.m. **c**, Representative 3D LSFM showing the spatial distribution of PMNs (Ly6G, green) and mononuclear phagocytes (tdTomato$^+$, red) in knee joints of *Cx3cr1^{cre}R26-tdTomato* mice at indicated time points upon induction of K/BxN STA (AF, grey). Filled arrowheads point towards the macrophage lining layer to highlight changes in its morphology upon induction of STA. Scale bars, 100 μm. **d**, Exemplary BFM images of the synovial membrane of knee joints of *Cx3cr1^{cre}R26-tdTomato* mice at day 0, day 2 and 7 after induction of STA. Macrophages are defined as tdTomato$^+$ (red) and F4/80$^+$ (white) and infiltrating neutrophils as Ly6G$^+$ (green) cells. Scale bars, 25 μm. **e**, Spinning disk confocal microscopy images of the synovial membrane of *Cx3cr1^{cre}R26-tdTomato* mice at day 2 after induction of K/BxN STA visualizing macrophages (tdTomato$^+$, red) and neutrophils (Ly6G, green). Scale bars, 10 μm. **f**, CLSM scans of the synovial membrane in knee joints of *ColVI^{cre}R26-tdTomato* reporter mice at the indicated time points after the induction of STA, enabling the visualization of synovial fibroblasts (tdTomato, red) and macrophages (CD68, green) along the synovial cavity (sc). Scale bars, 20 μm. **g**, LSFM of knee joints of *Cx3cr1^{cre}R26-tdTomato* mice showing the spatial distribution of macrophages (tdTomato, red) along the synovial cavity at day 21 after the first immunization during collagen-induced arthritis before the onset of arthritis (steady state) (top) and at day 35 after the first immunization after onset of joint inflammation, identifying rearrangement of macrophages in the form of palisade-like structures (filled arrowheads). Scale bars, 500 μm (left), 100 μm (right). AF, grey. **h**, CLSM images of knee joints of *Cx3cr1^{cre}R26-tdTomato* mice at day 21 (top; steady state before onset of arthritis) and day 35 (bottom; during active arthritis) of collagen-induced arthritis, illustrating reorganization of lining macrophages (tdTomato, red; CD68, green). Scale bars, 100 μm; scale bar of magnified view, 10 μm.

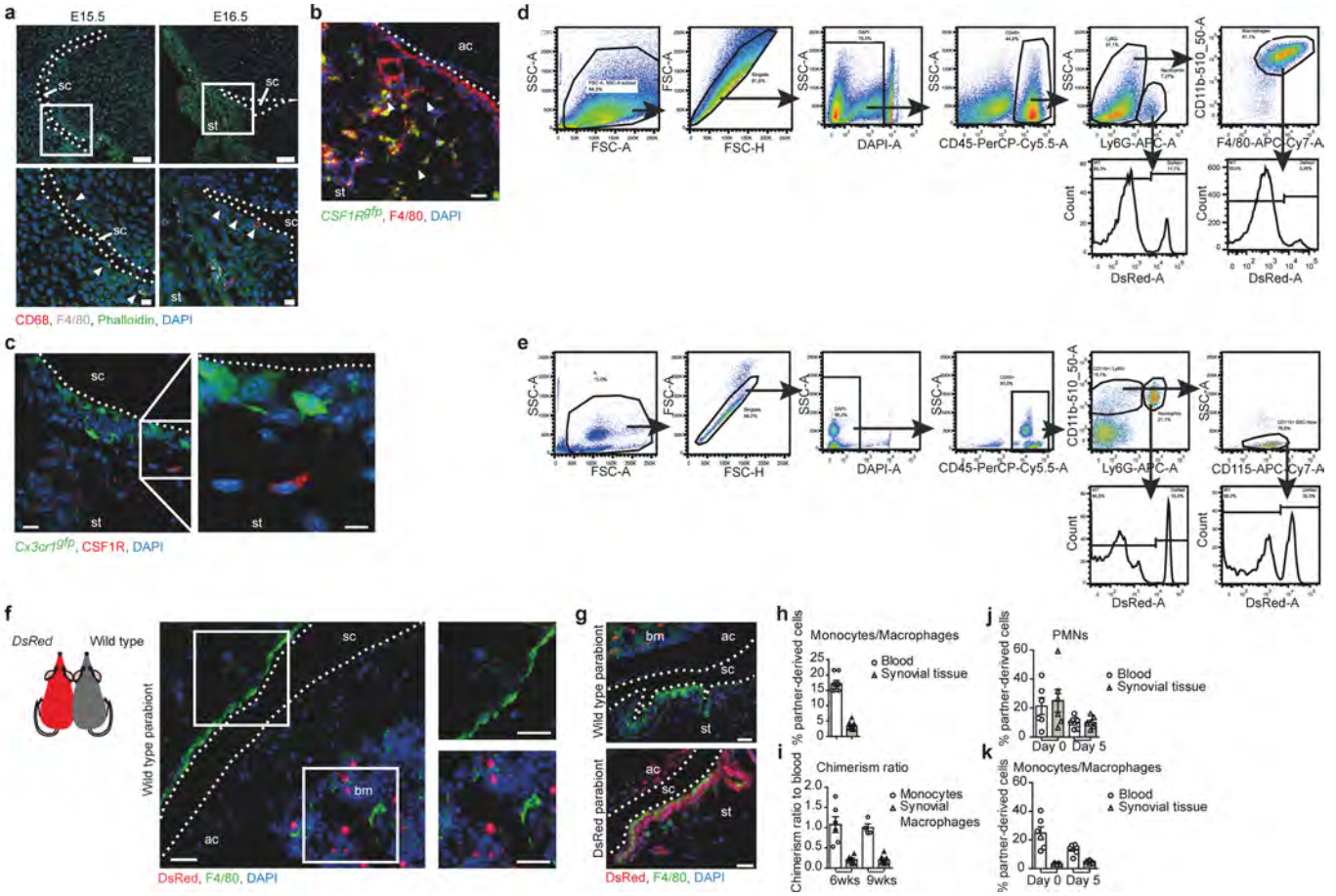

Extended Data Fig. 2 | Developmental origin of synovial lining macrophages. a, Histological CLSM analysis of embryonic mouse knee joints at E15.5 and E16.5 visualizing CD68 (red) and F4/80 (white) expressing embryonic macrophages (filled arrowheads) within the newly formed synovial lining. Scale bars, 50 μm (top), 10 μm (bottom). **b**, BFM showing expression of CSF1R and the distribution of macrophages (F4/80, red) within the synovial tissue of *CSF1R*^{GFP} mice (GFP, green; left). **c**, Representative CLSM scans of *Cx3cr1*^{GFP} (green) knee joints confirming the expression of CSF1R (red) by antibody-mediated staining on interstitial CX_3CR1^- macrophages. Scale bars, 25 μm, scale bar of magnified view, 10 μm. **d**, Gating strategy for analysis of synovial macrophages isolated from hind paws of parabiotic *DsRed*/wild-type mice. Synovial macrophages were defined as $DAPI^-$ living, $CD45^+$, $Ly6G^-$, $CD11b^+$, $F4/80^+$ cells. DsRed expression discriminates the origin. **e**, Gating strategy for blood monocytes of parabiotic *DsRed*/wild-type mice. Blood monocytes were defined as $DAPI^-$ living, $CD45^+$, $CD11b^+$, $Ly6G^-$, $CD115^+$ and SSC^{low}. DsRed expression discriminates the origin. **f**, Representative BFM of the synovial membrane of knee joints of a wild-type mouse sharing circulation with a *DsRed* mouse, six weeks after establishment of parabiosis ($n = 3$; DsRed, red; F4/80, green). Scale bars, 25 μm. **g**, BFM images of parabiotic wild-type (top) and *DsRed* (bottom) mice after nine weeks of parabiosis. In the wild-type mice, $DsRed^+$ partner-derived macrophages are visible in the bone marrow (bm), but not detected in the macrophage (F4/80, green) lining layer. Scale bars, 25 μm. **h**, Flow-cytometric analysis of the percentage of partner-derived blood monocytes and synovial macrophages of *DsRed*/wild-type parabionts after 9 weeks of parabiosis. Mean ± s.e.m. Blood, $n = 8$; synovial joint, $n = 8$. **i**, Chimerism ratio of blood monocytes and synovial macrophages in *DsRed*/wild-type parabionts after six weeks and nine weeks of parabiosis, calculated as the quotient of content of partner-derived tissue macrophages to partner-derived blood monocytes. A chimerism ratio of one represents the chimerism observed in blood monocytes. Mean ± s.e.m. Monocytes 6 weeks, $n = 6$; synovial macrophages 6 weeks, $n = 6$; monocytes 9 weeks, $n = 4$; synovial macrophages 9 weeks, $n = 8$. **j**, **k**, Flow-cytometric analysis of parabiotic hind paws of *DsRed*/wild-type parabionts at the indicated time points of K/BxN serum transfer arthritis. Data presented show the percentage of partner-derived PMNs (**k**) and monocytes/macrophages (**l**) within the blood circulation and the synovial tissue and are used to calculate the individual chimerism of tissue- and blood-derived cells. Mean ± s.e.m. For **j**, blood day 0 $n = 6$; synovial tissue day 0, $n = 6$; blood day 5, $n = 8$; synovial tissue day 5, $n = 7$. For **k**, blood day 0, $n = 6$; synovial tissue day 0, $n = 5$; blood day 5, $n = 7$; synovial tissue day 5, $n = 8$.

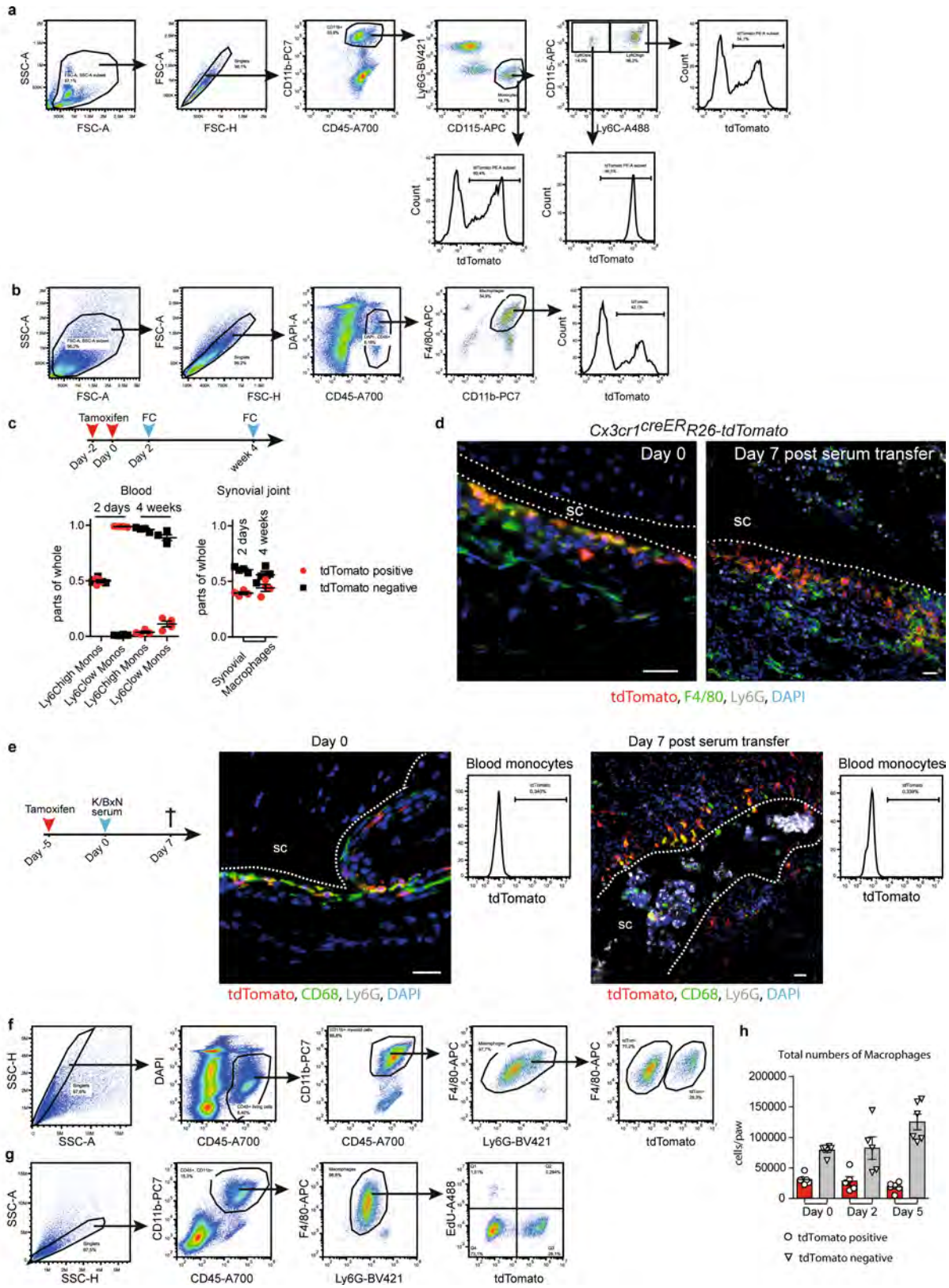

Extended Data Fig. 3 | See next page for caption.

Extended Data Fig. 3 | Fate mapping of synovial lining macrophages during arthritis. a, Gating strategy for $CD45^+CD11b^+Ly6G^-CD115^+$ classical $Ly6C^{high}$ and non-classical $Ly6C^{low}$ monocytes of *Cx3cr1*^{creER}*R26-tdTomato* mice. **b**, Gating strategy for $DAPI^-$ living, $CD45^+CD11b^+Ly6G^-F4/80^+$ macrophages of *Cx3cr1*^{creER}*R26-tdTomato* mice. **c**, Evaluation of tdTomato expression in blood monocytes and synovial macrophages two days and four weeks after tamoxifen pulse. Mean ± s.e.m.; $n = 4$ per group. **d**, **e**, BFM images of knee joint synovial membranes of *Cx3cr1*^{creER}*tdTomato* mice four weeks after systemic tamoxifen pulse (**d**) and five days after local injection of (*Z*)-4-hydroxytamoxifen (**e**) at day 0 and day 7 after the induction of K/BxN STA showing selective tdTomato (red) expression in synovial lining macrophages. The smaller graphs to the right in **e** show the absence of tdTomato expression in blood monocytes after local (Z)-4-hydroxytamoxifen injection. Scale bars, 25 μm. **f**, Gating strategy for $DAPI^-$ living, $CD45^+CD11b^+Ly6G^-F4/80^+$ macrophages of *Cx3cr1*^{creER}*R26-tdTomato* mice four weeks after tamoxifen pulse, used to calculate the absolute numbers of $tdTomato^+$ macrophages during steady state and K/BxN STA. **g**, Gating strategy after EdU labelling of proliferating macrophages ($CD45^+CD11b^+Ly6G^-$ $F4/80^+$) of *Cx3cr1*^{creER}*R26-tdTomato* mice. **h**, Quantification of total $tdTomato^+$ and $tdTomato^-$ macrophages in paws of *Cx3cr1*^{creER}*R26-tdTomato* mice 4 weeks upon tamoxifen pulse at day 0, 2 and 5 after induction of STA. Mean ± s.e.m. Day 0, $n = 6$; day 2, $n = 5$; day 5, $n = 6$.

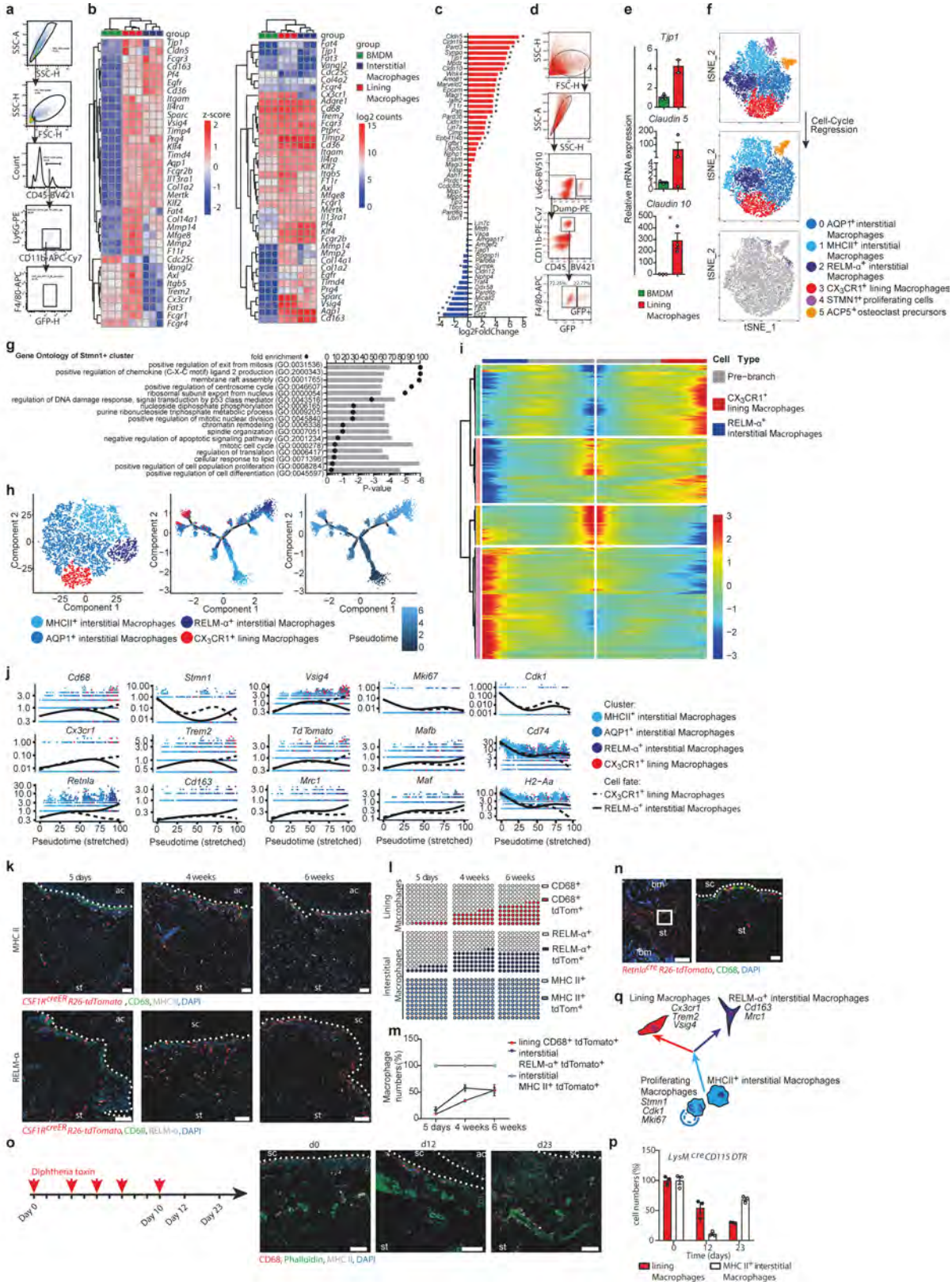

Extended Data Fig. 4 | See next page for caption.

Extended Data Fig. 4 | Transcriptional profiling of steady-state synovial macrophage subsets. a, Sorting strategy for bulk RNA sequencing analysis of synovial macrophages of *Cx3cr1*^{GFP} mice. Macrophages were defined as CD45$^+$, Ly6G$^-$, CD11$^+$ and F4/80$^+$. GFP discriminated GFP$^+$ lining macrophages and GFP$^-$ interstitial macrophages. **b**, Hierarchical clustering of *z*-score (left) and $\log_2$ counts (right) of selected genes of sorted GFP$^+$ lining macrophages, GFP$^-$ interstitial macrophages and BMDMs generated from bulk RNA sequencing. **c**, Differential gene expression (mean fold change, $\log_2$(differentially expressed genes) ($n = 3$ per group) of tight-junction-associated genes comparing CX_3CR1^+ lining macrophages and BMDMs. Differential expression was performed with DESeq2. A Wald test was used to calculate two-sided *P* values; adjustment for multiple comparisons was performed with the Benjamini–Hochberg method. $^*P \leq 0.05$. **d**, Sorting strategy for synovial macrophages of *Cx3cr1*^{GFP} mice for confirmatory quantitative analysis by PCR with reverse transcription (RT–PCR). Macrophages were defined as CD45$^+$, Ly6G$^-$, CD11$^+$ and F4/80$^+$. GFP discriminated GFP$^+$ lining macrophages and GFP$^-$ interstitial macrophages. A dump channel using anti-CD31 and anti-E-cadherin was integrated to avoid endothelial cell or epithelial cell contaminations. **e**, Confirmatory quantitative RT–PCR analysis in synovial macrophage subsets determining expression of mRNAs encoding TJP1 (BMDM, $n = 3$; lining macrophage, $n = 2$), claudin 5 ($n = 3$ per group) and claudin 10 ($n = 3$ per group) in sorted GFP$^+$ lining macrophages and in vitro cultured BMDMs, mean ± s.e.m.; two-tailed Student's *t*-test, $^*P = 0.012$. **f**, *t*-SNE profile of sorted synovial CD45$^+$CD11b$^+$Ly6G$^-$ mononuclear phagocytes of *Cx3cr1*^{creER}*R26-tdTomato* mice analysed four weeks after tamoxifen pulse during steady-state conditions (top). After clustering, cell-cycle phase scoring based on canonical markers and regression was performed to determine clustering independent of cell cycle phase (middle and bottom). $n = 7{,}362$ cells. **g**, Gene ontology enrichment analysis of biological processes in cells of the proliferating *Stmn1*$^+$ cluster of sorted CD45$^+$CD11b$^+$Ly6G$^-$ mononuclear phagocytes of a healthy tamoxifen-pulsed *Cx3cr1*^{creER}*R26-tdTomato* mouse. The top 51 cluster marker genes determined with Seurat were used to perform a PANTHER overrepresentation test. The list of markers for the *Stmn1*$^+$ cluster was compared to the reference list using Fisher's exact test with false discovery rate correction. **h**, *t*-SNE profile of sorted synovial CD45$^+$CD11b$^+$Ly6G$^-$ mononuclear phagocytes of a healthy tamoxifen-pulsed *Cx3cr1*^{creER}*R26-tdTomato* mouse after excluding *Acp5*$^+$ osteoclast precursors revealing four remaining clusters (left). Single-cell trajectory analysis integrating cluster information (middle) and pseudotime (right) show a branch point of cellular differentiation into lining macrophages (red) or interstitial *Retnla*$^+$ macrophages (dark blue) starting from proliferating MHCII$^+$ macrophages (light blue). $n = 7{,}028$ cells. **i**, Differential gene expression analysis as a function of pseudotime in a branch-dependent manner showing a common gene signature of a pre-branch precursor cell population choosing two main cell fates: either *Cx3cr1*$^+$ lining macrophage or interstitial *Retnla*$^+$ macrophage. **j**, Gene expression changes of selected marker genes as a function of pseudotime reflecting the cellular differentiation into *Retnla*$^+$ interstitial macrophages (solid line) and *Cx3cr1*$^+$ lining macrophages (dashed line). $n = 7{,}028$ cells. **k**, BFM images of knee joints of *Csf1r*^{creER}*R26-tdTomato* mice (tdTomato, red) determining tdTomato expression in CD68$^+$ (green) lining macrophages, MHCII$^+$ interstitial macrophages (MHCII, white; top) and RELM-α$^+$ interstitial macrophages (RELM-α, white; bottom) at indicated times after the start of tamoxifen treatment. Scale bars, 50 μm. **l**, **m**, Quantification of relative changes in tdTomato$^+$ cells among CD68$^+$ lining macrophages, RELM-α$^+$ interstitial macrophages and MHCII$^+$ interstitial macrophages in *Csf1r*^{creER}*R26-tdTomato* mice at indicated times after the start of tamoxifen treatment. $n = 3$ mice per group. Data are mean ± s.e.m. **n**, tdTomato (red) expression in CD68$^+$ (green) macrophages in synovial tissue of the knee joint of *Retnla*^{cre}*R26-tdTomato* mice. Scale bars, 250 μm (left), 25 μm (right). **o**, **p**, BFM images (**o**) and quantification of changes (**p**) in CD68$^+$ (red) lining macrophages and MHCII$^+$ (white) interstitial macrophages in *LysM*^{cre}*CD115DTR* mice after 10 days of DT treatment, at the indicated time points after the beginning of DT treatment. Scale bars, 50 μm. $n = 3$ technical replicates. Data are mean ± s.e.m. **q**, Scheme of the postulated dynamic continuum of differentiating tissue-resident macrophages within the synovial tissue.

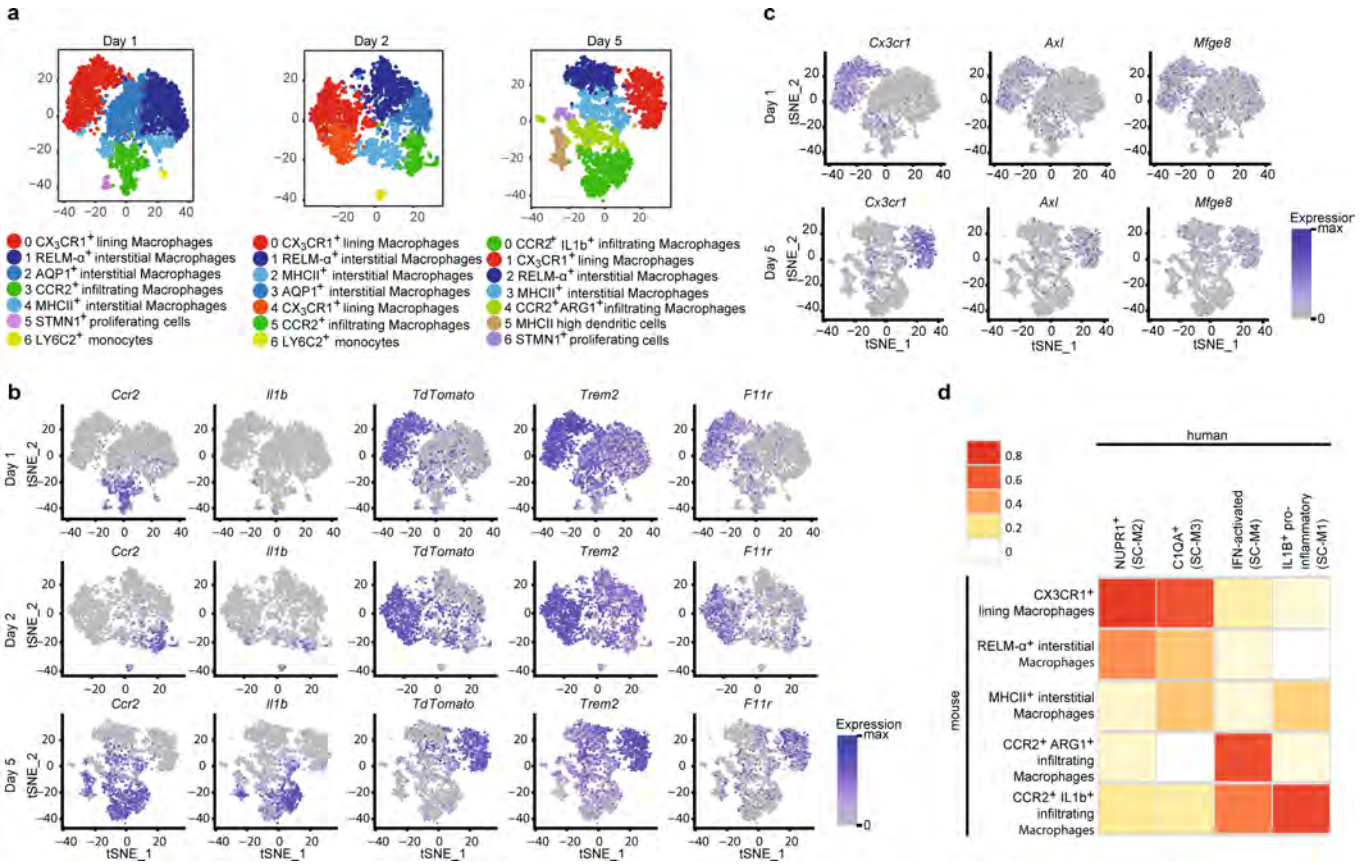

Extended Data Fig. 5 | Transcriptional profiling of mononuclear phagocytes during arthritis. a, *t*-SNE scRNA-seq profiles of sorted synovial CD45$^+$CD11b$^+$Ly6G$^-$ mononuclear phagocytes of *Cx3cr1*^{creER}*R26-tdTomato* mice analysed four weeks after tamoxifen pulse at the indicated time points after the induction of K/BxN STA, coloured by cluster assignment and annotated post hoc. Day 1, $n = 4{,}640$ cells; day 2, $n = 2{,}722$ cells; day 5, $n = 3{,}237$ cells. **b**, scRNA-seq-derived expression patterns of indicated genes within synovial mononuclear phagocytes at indicated time points after the induction of STA. Day 1, $n = 4{,}640$ cells; day 2, $n = 2{,}722$ cells; day 5, $n = 3{,}237$ cells. **c**, *t*-SNE plots of sorted CD45$^+$CD11b$^+$Ly6G$^-$ cells from arthritic hind paws at day 1 and day 5 after K/BxN serum transfer, showing the expression of *Cx3cr1*, *Axl* and *Mfge8* within the cluster of lining macrophages. **d**, Comparison of available scRNA-seq datasets from monocytes of human synovial tissue derived from patients suffering from rheumatoid arthritis and osteoarthritis[8] with scRNA-seq profiles of mouse CD45$^+$CD11b$^+$Ly6G$^-$ cells on day 5 after the induction of STA. Values represent the quotient of the numbers of all co-expressed marker genes of the 5 macrophage clusters at day 5 to the top 20 provided human marker genes of the 4 described subpopulations of human monocytes SC-M1, SC-M2, SC-M3 and SC-M4.

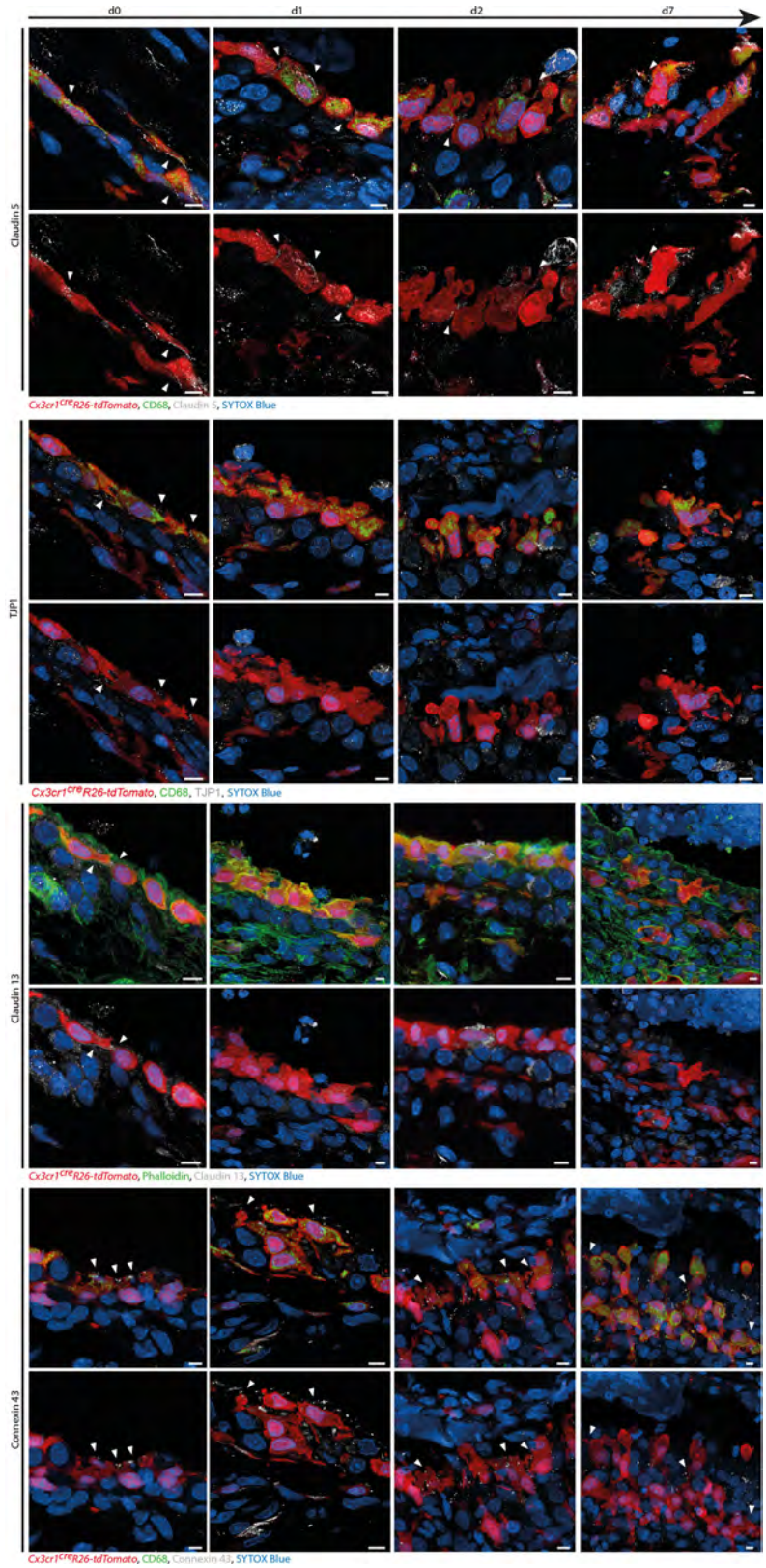

Extended Data Fig. 6 | Expression patterns of tight-junction proteins and gap-junction proteins in tdTomato$^+$ lining macrophages. Expression of claudin 5, TJP1/ZO-1 and claudin 13 as well as that of connexin 43 (grey, filled arrowheads) in synovial lining tdTomato$^+$ (red) macrophages of *Cx3cr1^{cre}R26-tdTomato* mice during steady state and on days 1, 2 and 7 after the induction of K/BxN STA. Scale bars, 5 μm.

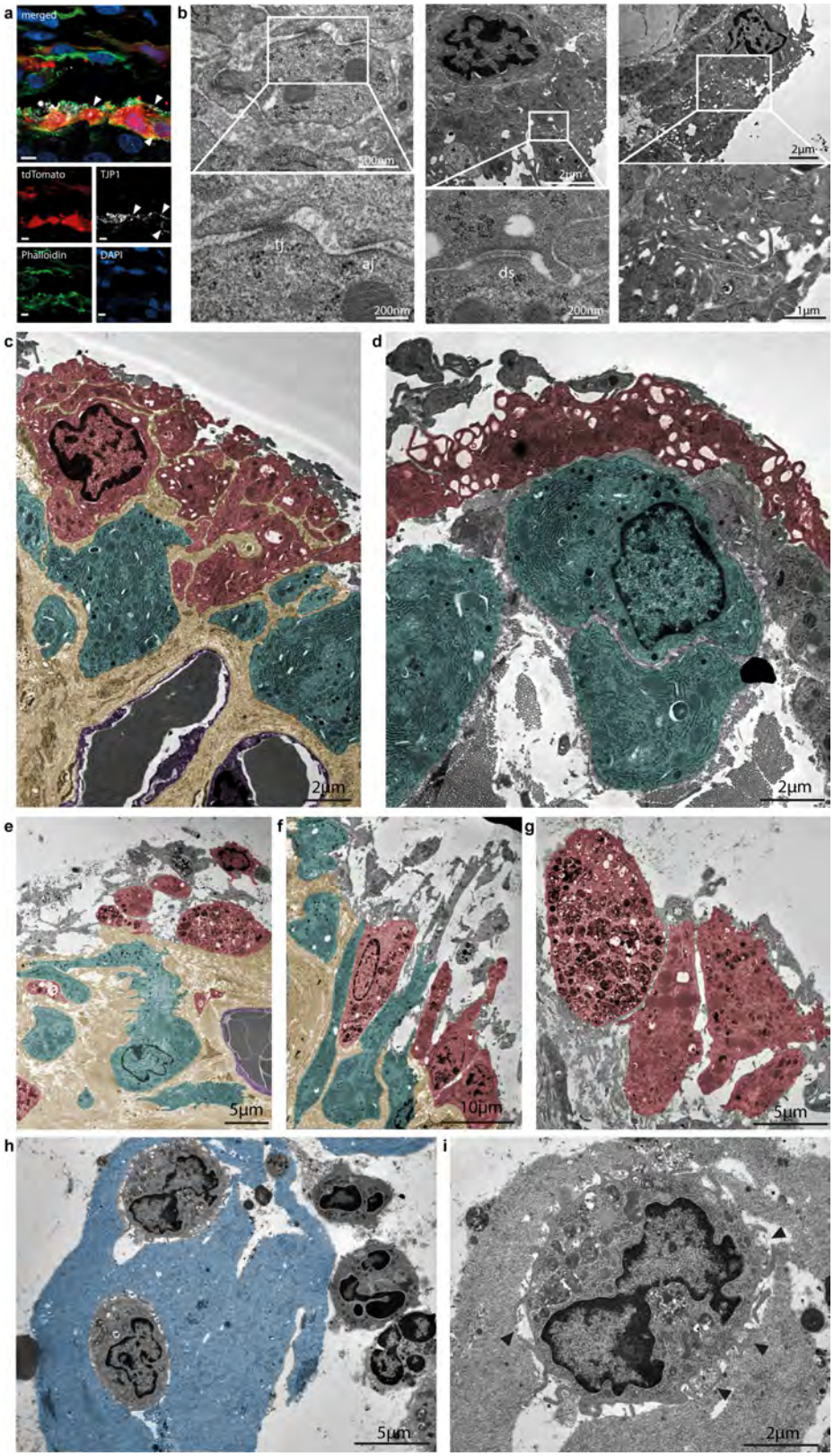

Extended Data Fig. 7 | See next page for caption.

Extended Data Fig. 7 | Ultrastructural characterization of cell–cell contacts between lining macrophages. a, Representative CLSM of macrophages (tdTomato, red) within the synovial membrane of knee joints of *Cx3cr1*^{creER}*R26-tdTomato* mice, visualizing the tight-junction protein ZO-1/TJP1 (white). Phalloidin, green; DAPI, blue. Scale bars, 5 μm. **b**, Transmission electron microscopy (TEM) images of the synovial membrane of a healthy knee joint showing tight junctions (tj), adherens junctions (aj), desmosomes (ds) and interdigitations connecting synovial lining macrophages. **c**, TEM micrograph showing synovial lining macrophages (red) constituting a dense physical barrier segregating the synovial fluid from sublining interstitial tissue containing synovial fibroblasts (cyan), endothelial cells (purple) embedded into the extracellular matrix (beige). **d**, TEM micrograph demonstrating synovial macrophages (red) forming the uppermost cell layer covering the layer of synovial fibroblasts (cyan). **e**, **f**, TEM micrographs of an inflamed synovial membrane two days after induction of K/BxN STA, showing the disruption of the covering synovial macrophage (red) layer and a reorientation of synovial macrophages (red) and synovial fibroblasts (cyan) directed to the synovial cavity. **g**, A TEM micrograph of an inflamed synovial membrane two days after the induction of STA reveals the emergence of macrophages containing large amounts of vacuoles filled with phagocytosed material. **h**, **i**, Recruited monocytes and granulocytes as well as free DNA of neutrophil extracellular traps (blue) within the synovial cavity of knee joints two days after the induction of STA. Filled arrowheads point at an exemplary monocyte engulfing free DNA.

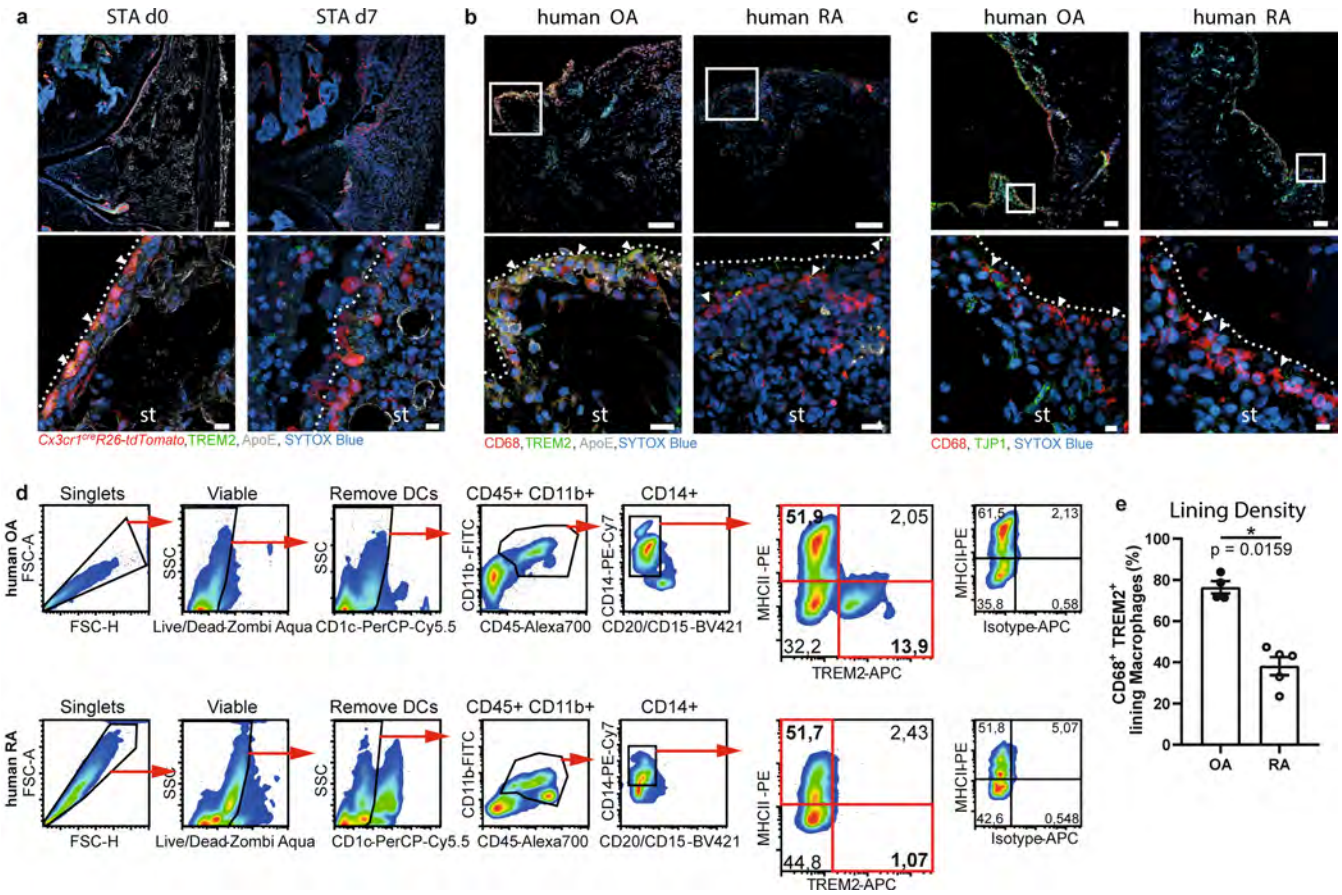

Extended Data Fig. 8 | Comparison of mouse and human synovial lining macrophages. a, Histological sections of healthy (STA day 0, left) and inflamed (STA day 7, right) mouse knee joints of *Cx3cr1*^{cre}*R26-tdTomato* mice, showing the expression of TREM2 (green; filled arrowheads) in lining macrophages (tdTomato, red). Scale bars, 100 μm (top), 10 μm (bottom). **b**, **c**, Histological sections of synovial tissue of human knee joints isolated from patients diagnosed with osteoarthritis (OA) and rheumatoid arthritis (RA) determining expression of TREM2 (green; filled arrowheads) (**b**) and TJP1 (green; filled arrowheads) (**c**) in synovial macrophages (CD68, red). Scale bars, 100 μm (top), 10 μm (bottom). **d**, Flow-cytometric analysis of the composition and frequencies of MHCII^{+}TREM2^{-} and MHCII^{-}TREM2^{+} mononuclear phagocytes in synovial tissue samples isolated from human knee joints of patients diagnosed with osteoarthritis and rheumatoid arthritis. **e**, Histology-based quantification of the density of the synovial macrophage lining (defined as percentage of CD68^{+}TREM2^{+} macrophages among total lining cells) in synovial tissue sections of patients diagnosed with osteoarthritis ($n = 4$) and rheumatoid arthritis ($n = 5$), respectively. Data are mean ± s.e.m., two-tailed Student's *t*-test.

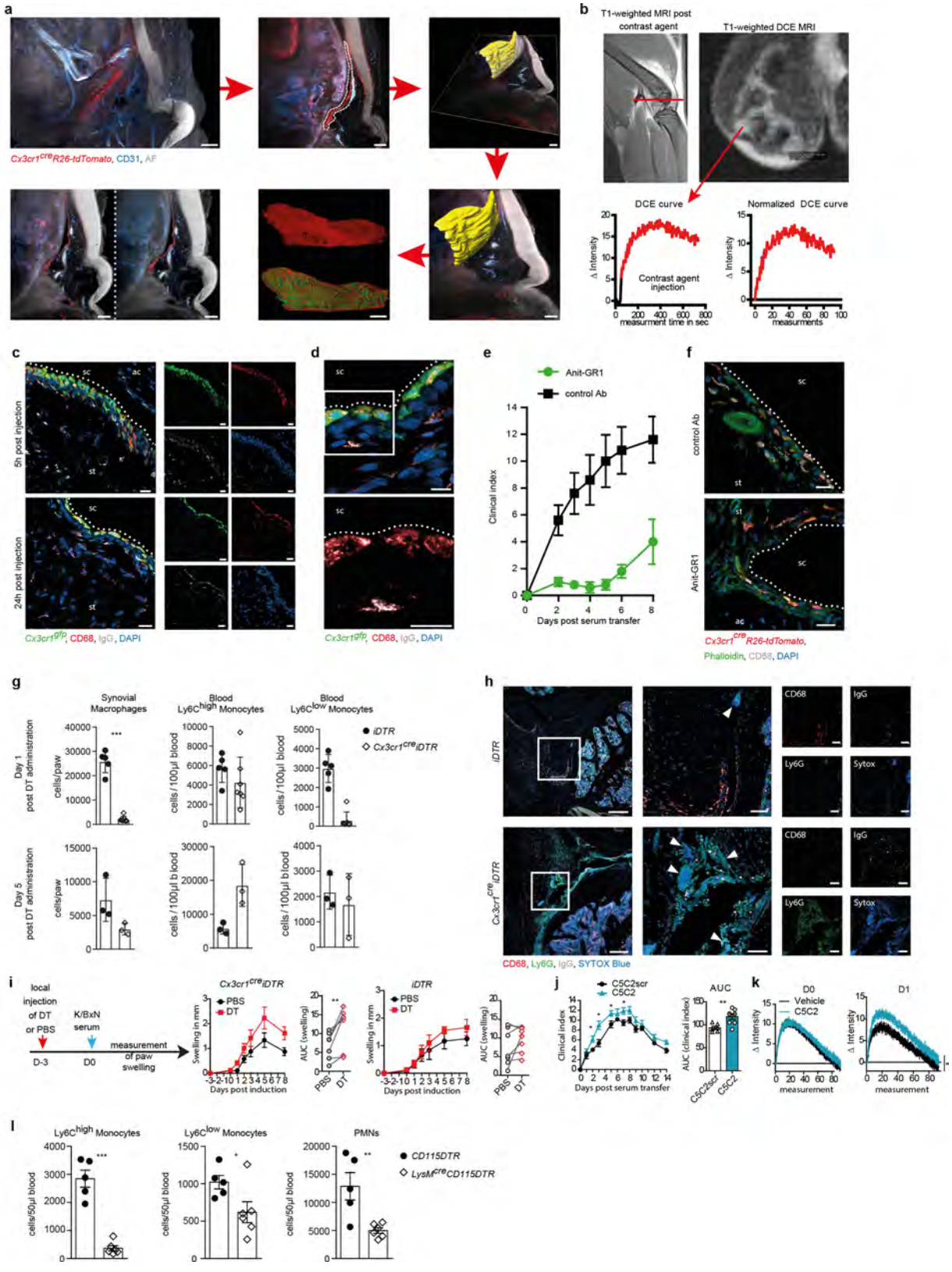

Extended Data Fig. 9 | See next page for caption.

Extended Data Fig. 9 | Role of CX_3CR1^+ macrophages during arthritis. **a**, To quantify lining density, tdTomato$^+$ macrophages (red) were manually isolated from 3D reconstructions of optically cleared and LSFM-imaged *Cx3cr1^{cre}R26-tdTomato* knee joints (autofluorescence, grey; CD31, blue) using Imaris software. Isolated surfaces (yellow) were volume-rendered for tdTomato$^+$ macrophages (red) and whole-area volume (green). Lining density was calculated from the ratio of whole-area volume to macrophage volume. An exemplary image of the same knee joint before and after isolation of lining macrophages is shown. Scale bars, 200 μm. **b**, Dynamic-contrast-enhanced magnetic resonance imaging (DCE-MRI) data analysis. The red line drawn in the sagittal T1-weighted image after administration of contrast agent marks the transverse plane used for T1-weighted DCE-MRI analysis. The DCE curve generated from the region of interest (synovial tissue) was normalized to the measurement time point after complete injection of contrast agent, and the time of measurements was converted to distinctive measurements. **c**, CLSM images of knee joints of *Cx3cr1^{GFP}* mice injected with protein-G-purified and Alexa-Fluor-647-labelled K/BxN serum IgG (grey) at the indicated time points after IgG injection, determining the uptake of labelled IgG by macrophages (GFP, green; CD68, red) in the synovial tissue and the synovial lining (synovial cavity, sc). Scale bars, 10 μm. **d**, CLSM scan with higher magnification showing localization of labelled IgG (grey) inside the vacuoles of CD68$^+$ (red) lining and interstitial synovial macrophages 24 h after injection. Scale bars, 10 μm. **e**, Clinical course of K/BxN STA in wild-type mice that were treated with an anti-GR1 antibody to deplete PMNs and inflammatory Ly6C^{high} monocytes and a control antibody (LTF-2), one day before induction of STA. Mean ± s.e.m.; $n = 5$ per group. **f**, Histological CLSM analysis of lining morphology after anti-GR1 antibody-mediated neutrophil/monocyte depletion one day after induction of STA. Lining macrophages (tdTomato, red). Scale bars, 20 μm. **g**, Flow cytometry analysis of synovial macrophages and blood Ly6C^{high} or Ly6C^{low} monocytes of *Cx3cr1^{cre}iDTR* mice and *iDTR* control mice one day and five days after two injections of DT (500 ng per mouse per day, i.p.). Mean ± s.e.m; For day 1: *iDTR*, $n = 5$; *Cx3cr1^{cre}iDTR*, $n = 7$; for day 5, $n = 3$ per group. Two-tailed Student's *t*-test, $***P < 0.0001$. **h**, Representative BFM images of the infiltration of PMNs (Ly6G, green) and neutrophil extracellular trap formation (filled arrowheads, DAPI, blue) within the synovial cavity of knee joints of *Cx3cr1^{cre}iDTR* ($n = 3$) and *iDTR* control ($n = 3$) mice 6 days after injection of DT and 24 h after induction of STA (CD68, red). Scale bars, 200 μm and for magnified view, 50 μm. **i**, Treatment scheme and clinical course of STA in *Cx3cr1^{cre}iDTR* and *iDTR* control mice that had received a unilateral local injection of DT ($n = 7$) and PBS ($n = 7$), respectively. *P* values calculated using two-tailed paired *t*-test, $**P = 0.008$. **j**, Clinical course of STA including AUC of the corresponding clinical index in C57BL/6 wild-type mice treated with C5C2 claudin peptidomimetics (3.5 μmol kg^{-1}, i.v., $n = 8$) or scrambled C5C2 control peptide (C5C2scr; 3.5 μmol kg^{-1}, i.v., $n = 6$) one day before and after the induction of STA. Data are mean ± s.e.m. Mann–Whitney *U*-test for clinical index with $*P \leq 0.05$, and two-tailed Student's *t*-test for AUC with $**P = 0.0062$. **k**, Normalized signal intensity curves of DCE-MRI of synovial tissue of knee joints over 90 measurements with intervals of 7 s at the indicated days after STA in C57BL/6 wild-type mice treated with C5C2 claudin peptidomimetics (3.5 μmol kg^{-1}, i.v.) or vehicle one day before the induction of STA. Data are mean ± s.e.m. Day 0: vehicle, $n = 10$ knee joints; C5C2, $n = 10$ knee joints; day 1: vehicle, $n = 9$ knee joints; C5C2, $n = 10$ knee joints. *P* values for AUC were calculated using two-tailed Student's *t*-test, $*P = 0{,}0256$. **l**, Flow cytometry of blood monocytes and neutrophils of *LysM^{cre}CD115DTR* mice ($n = 6$) and *CD115DTR* control mice ($n = 5$) one day after two injections of DT (500 ng per mouse per day, i.p.). Mean ± s.e.m.; two-tailed Student's *t*-test, $*P = 0.0467$, $**P \leq 0.0069$, $***P = 0.0001$.

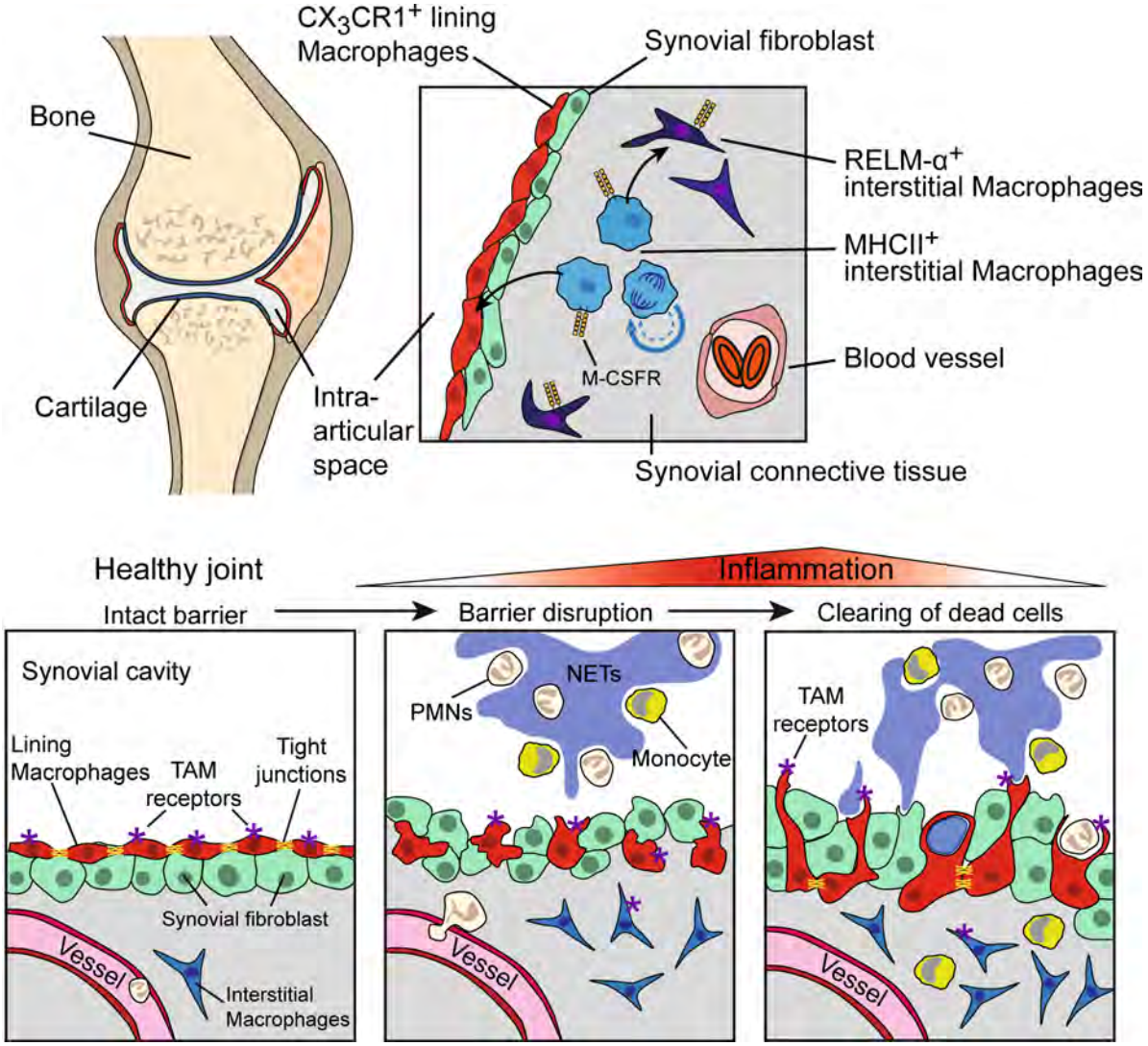

Extended Data Fig. 10 | Schematic summary. Top, scheme of the postulated origin of resident synovial CX_3CR1^+ lining macrophages that constantly repopulate from proliferating tissue resident $CX_3CR1^-MHCII^+$ interstitial macrophages. Bottom, tight-junction-forming resident lining macrophages form a protective barrier for joint structures that disintegrates during arthritis, enabling infiltration of inflammatory myeloid cells.

nature research

Corresponding author(s): G. Krönke, S. Culemann, A. Grüneboom

Reporting Summary

Nature Research wishes to improve the reproducibility of the work that we publish. This form provides structure for consistency and transparency in reporting. For further information on Nature Research policies, see Authors & Referees and the Editorial Policy Checklist.

Statistical parameters

When statistical analyses are reported, confirm that the following items are present in the relevant location (e.g. figure legend, table legend, main text, or Methods section).

n/a	Confirmed	
☐	☒	The exact sample size (*n*) for each experimental group/condition, given as a discrete number and unit of measurement
☐	☒	An indication of whether measurements were taken from distinct samples or whether the same sample was measured repeatedly
☐	☒	The statistical test(s) used AND whether they are one- or two-sided *Only common tests should be described solely by name; describe more complex techniques in the Methods section.*
☒	☐	A description of all covariates tested
☐	☒	A description of any assumptions or corrections, such as tests of normality and adjustment for multiple comparisons
☐	☒	A full description of the statistics including central tendency (e.g. means) or other basic estimates (e.g. regression coefficient) AND variation (e.g. standard deviation) or associated estimates of uncertainty (e.g. confidence intervals)
☒	☐	For null hypothesis testing, the test statistic (e.g. *F*, *t*, *r*) with confidence intervals, effect sizes, degrees of freedom and *P* value noted *Give P values as exact values whenever suitable.*
☒	☐	For Bayesian analysis, information on the choice of priors and Markov chain Monte Carlo settings
☒	☐	For hierarchical and complex designs, identification of the appropriate level for tests and full reporting of outcomes
☒	☐	Estimates of effect sizes (e.g. Cohen's *d*, Pearson's *r*), indicating how they were calculated
☐	☒	Clearly defined error bars *State explicitly what error bars represent (e.g. SD, SE, CI)*

Our web collection on statistics for biologists may be useful.

Software and code

Policy information about availability of computer code

Data collection	Leica TCS SP 5 II CLSM data were collected using Las AF software version 2.7.3.9723. Spinning Disc Confocal Microscopy (SDCM) was eprfomred by using a Zeiss Spinning Disc Axio Observer.Z1 and images were collected via the Zen Blue image aquisition software Version 2.3. Light sheet fluorescence microscopy (LSFM) data were generated using an Ultramicrospe II (LaVision BioTech GmbH) and collected with Imspector software Version 5.1.304. MRI scans were performed using a ClinScan 70/30 7 Tesla MRI System (Bruker). Flow cytometry data and cell sorting data were aquired by using a CytoFLex S (Beckman Coulter) and a MoFlo XDP (Beckman Coulter) system. Individual settings for data acquisitions via the systems listed above are described in detail in the experimental procedures.
Data analysis	CLSM and SDCM data were processed and analysed using huygens professional software Version 17.10 (Scientific Volume Imaging), Imaris software Version 9.1 (Bitplane) and Image J software Version 1.8.0_112. LSFM data were processed using Imaris software Version 9.1 (Bitplane) and Image J software version 1.8.0_112. MRI data were processed via Horos LGPL Version 3.0. Flow cytometry data and cell sorting data were analyzed via the Summit Software System, MacsQuantify (Miltenyi Biotec, Version 2.5), CytExpert (Beckman Coulter, Version 2.2.0.97), FlowJo (FlowJo, Version 7.6.5), and Kaluza software (Beckman Coulter, Version 1.5a). Statistical data analysis was performed with GraphPad Prism 5.

Differential expression analysis was performed with the DESeq2 package v.1.20.0 and volcano plots were generated with ggplot2 package in R software.
For single cell RNA sequencing analysis CellRanger 2.1.0, FastQC v0.11.7, the Seurat (Version 2.3) package for R and Monocle 2 package were used.

All data analysis strategies and softwares are described prescisely in the experimental procedures and supplementary table 3.

For manuscripts utilizing custom algorithms or software that are central to the research but not yet described in published literature, software must be made available to editors/reviewers upon request. We strongly encourage code deposition in a community repository (e.g. GitHub). See the Nature Research guidelines for submitting code & software for further information.

Data

Policy information about availability of data

All manuscripts must include a data availability statement. This statement should provide the following information, where applicable:

- Accession codes, unique identifiers, or web links for publicly available datasets
- A list of figures that have associated raw data
- A description of any restrictions on data availability

The data that support the findings of this study are available on reasonable request from the corresponding author [G.K, S.C., A.G.]. The data are not publicly available due to comprised information that could compromise research participant privacy.

Field-specific reporting

Please select the best fit for your research. If you are not sure, read the appropriate sections before making your selection.

☒ Life sciences ☐ Behavioural & social sciences ☐ Ecological, evolutionary & environmental sciences

For a reference copy of the document with all sections, see nature.com/authors/policies/ReportingSummary-flat.pdf

Life sciences study design

All studies must disclose on these points even when the disclosure is negative.

Sample size	Sample size was determined by statistical power analysis including high signficance levels ($p < 0.05$). For calculation of statistical significance GraphPad Prism 5 was used. Data are presented as mean ± SEM and were analyzed using Student's t-test, Mann-Whitney U-Test, or Kruskal-Wallis H-Test with Dunn's multiple comparisons test as post hoc procedure. P values less than 0.05 were considered significant. Differential expression analysis for Bulk RNA sequencing has been performed with DESeq2. Wald test was used to calculate two-sided p-values; adjustment for multiple comparisons was performed with the Benjamini-Hochberg method. For PANTHER Overrepresentation Test Fisher's exact Test with False Discovery Rate correction. Cluster markers of SingleCell Sequencing data sets were identified using the Wilcoxon Rank Sum test. Adjusted p-values based on Bonferroni correction using all genes in the dataset.
Data exclusions	No data were excluded from analysis.
Replication	Minimum three independent measurements per experiment were performed and successfully confirmed results.
Randomization	Experimental groups were randomly allocated. Treated groups were housed together with control groups.
Blinding	Data analysis was performed in a blinded fashion. The results were confirmed by two investigators, who analyzed the blindet data independently.

Reporting for specific materials, systems and methods

Materials & experimental systems

n/a	Involved in the study
[ ]	[x] Unique biological materials
[ ]	[x] Antibodies
[x]	[ ] Eukaryotic cell lines
[x]	[ ] Palaeontology
[ ]	[x] Animals and other organisms
[ ]	[x] Human research participants

Methods

n/a	Involved in the study
[x]	[ ] ChIP-seq
[ ]	[x] Flow cytometry
[x]	[ ] MRI-based neuroimaging

Unique biological materials

Policy information about availability of materials

Obtaining unique materials

All unique biological materials (genetically modified mouse strains) are available from standard commercial sources:

- C57BL/6J
Charles River
632

- C57BL/6Rj
Janvier Labs

- Tg(Cx3cr1-cre)MW126Gsat/Mmucd MMRRC
036395-UCD

- B6;129S6-Gt(ROSA)26Sortm9(CAG-tdTomato)Hze/J The Jackson Laboratory
007905

- STOCK Tg(ACTB-DsRed*MST)1Nagy/J, DsRed.T3 The Jackson Laboratory
005441

- B6.129P2(C)-Cx3cr1tm2.1(cre/ERT2)Jung/J The Jackson Laboratory
020940

- FVB-Tg(Csf1r-cre/Esr1*)1Jwp/J The Jackson Laboratory
019098

- C57BL/6-Gt(ROSA)26Sortm1(HBEGF)Awai/J
The Jackson Laboratory
007900

- B6;129S6-Gt(ROSA)26Sortm9(CAG-tdTomato)Hze/J The Jackson Laboratory
007905

- C57BL/6-Tg(Csf1r-HBEGF/mCherry)1Mnz/J The Jackson Laboratory
024046

- B6.129P-Cx3cr1tm1Litt/J The Jackson Laboratory
005582

All used mouse strains are additionally listed in supplementary table 1.

Antibodies

Antibodies used

Antibodies used in this study are:

- ApoE
unconjugated, Thermo Fisher, Cat: 701241, Lot: 1984882, Clone: 16H22L18, Dilution: 1:200

- CD1c-PerCP/Cy5.5
BioLegend, Cat: 331513, Lot: B267879, Clone: L161, Dilution: 1:500

- CD11b-PE/Cy7
BioLegend, Cat: 101216, Lot: B185646, Clone: M1/70, Dilution: 1:500

- CD11b-Alexa Fluor 488

BioLegend, Cat: 393107, Lot: B261594, Clone: LM2, Dilution: 1:500

- CD 14 PE-Cy7
BioLegend, Cat: 367111, Lot: B252403, Clone: 63D3, Dilution: 1:500

- CD15-Brilliant Violet 421
BioLegend, Cat: 232039, Lot: B263781, Clone: W6D3, Dilution: 1:500

- CD20-Brilliant Violet 421
BioLegend, Cat: 302329, Lot: B257594, Clone: 2H7, Dilution: 1:500

- CD31-PE
Biolegend, Cat:102507, Lot: B129965, Clone: MEC13.3, Dilution: 1:500

- CD31-Alexa Fluor 647
Biolegend, Cat: 102516, Lot: B234197, Clone: MEC13.3, Dilution: 2.5µg/mouse

- CD45-BrilliantViolet 421,
Biolegend, Cat:103133, Lot: B263588, Clone: 30-F11, Dilution: 1:500

- CD45-Alexa Fluor 700,
Biolegend, Cat: 368513, Lot: B248833, Clone: 2D1, Dilution: 1:500

- CD45.2-Alexa Flour 700
BioLegend, Cat: 109822, Lot: B202497, Clone: 104, Dilution: 1:500

- CD68-Alexa Fluor 594
BioLegend, Cat: 137020, Lot: B239125, Clone: FA-11, Dilution: 1:400

- CD68-Alexa Fluor 647
BioLegend, Cat: 137004, Lot: B153907, Clone: FA-11, Dilution: 1:400

- CD68 unconjugated
BioLegend, Cat: 333801, Lot: B200949, Clone: Y1/82A, Dilution: 1:200

- CD68 unconjugated
Abcam, Cat: ab955, Lot: GR3230929-1, Clone: KP1, Dilution: 1:200

- CD68 -Alexa Fluor 594
R&D systems, Cat: IC20401T, Lot: 1471045, Clone: 298807, Dilution: 1:200

- CSF1R-APC
Biolegend, Cat: 135510, Lot: B183456, Clone: AFS98, Dilution: 1:500

- CSF1R-Alexa Fluor 647
Biolegend, Cat: 135530, Lot: , Clone: AFS98, Dilution: 1:200

- Claudin 2 unconjugated
Abcam, Cat: ab53032, Lot: GR314368-11, Clone: polyclonal, Dilution: 1:200

- Claudin 5 unconjugated
Abcam, Cat: ab15106, Lot: GR3182385, Clone: polyclonal, Dilution: 1:200

- Claudin 13 unconjugated
Invitrogen, Cat: PA1-24420, Lot: TA2507851, Clone: polyclonal, Dilution: 1:200

- Connexin 43 unconjugated
Sigma Aldrich, Cat: C6219, Lot: 027144804V, Clone: polyclonal, Dilution: 1:200

- Donkey anti-Rabbit IgG Alexa Fluor 647
Life Technologies, Cat: A-31573, Lot: 1563697, Clone: polyclonal, Dilution: 1:200

- Donkey anti-Rabbit IgG Alexa Fluor 488
Life Technologies, Cat: A-21206, Lot: 1644644, Clone: polyclonal, Dilution: 1:200

- E-Cadherin-PE,
Biolegend, Cat: 147303, Lot: B260705, Clone: DECMA-1, Dilution: 1:500

- F4/80-Alexa Fluor 647,
BioLegend, Cat: 123122, Lot: B212680, Clone: BM8, Dilution: 1:400

- F4/80-FITC,
BioLegend, Cat: 123108, Lot: B177257, Clone: BM8, Dilution: 1:400

- HLA-DR PE,

BioLegend, Cat: 361605, Lot: B261328, Clone: Tü36, Dilution: 1:500

- Ki67-Af647,
BioLegend, Cat: 652407, Lot: B238782, Clone: 16A8, Dilution: 1:200

- Ly6C-Alexa Flour 488,
BioLegend, Cat: 128022, Lot: B248739, Clone: HK1.4, Dilution: 1:400

- Ly6G-Brilliant Violet,
BioLegend, Cat: 127627, Lot: B193096, Clone: 1A8, Dilution: 1:400

- Ly6G-FITC,
BioLegend, Cat: 127606, Lot: B175677, Clone: 1A8, Dilution: 1:400

- Ly6G-Alexa Fluor 488,
BioLegend, Cat: 127626, Lot: B240194, Clone: 1A8, Dilution: 1:400

- Ly6G-Alexa Fluor 647,
BioLegend, Cat: 127610, Lot: B204928, Clone: 1A8, Dilution: 1:200

- MHC II-PE,
Biolegend, Cat: 107608, Lot: B130064, Clone: M5/114.15.2, Dilution: 1:200

- Relm alpha
Abcam, Cat: ab39626, Lot: GR1287151, Clone: polyclonal, 1:200

- Trem 2 unconjugated
Abcam, Cat: ab86491, Lot: GR3207091-11, Clone: RM0139-5J46, Dilution: 1:200

- Trem2-APC,
R&D systems, Cat: FAB17291A, Lot: AADSO17111, Clone: 237920, Dilution: 1:500

- ZO-1 unconjugated, EMD Millipore, Cat: AB2272, Lot: 2905383, Clone: polyclonal, Dilution: 1:100

All used antibodies are listed in more detail in supplementary table 2, including information regarding antigen, conjugation, concentration, isotype, host reactivity, clone, source, Cat#, Lot#, dilution, and application.

Validation

Exclusively comercially available antibodies were used. Antibody specivicity, concentration and quality validation were performed by the manufacturers. Validation statements of the manufacturers can be found on their webpages:

- Abcam: https://www.abcam.com/primary-antibodies/improving-reproducibility-with-better-antibodies
- Biolegend: https://www.biolegend.com/reproducibility
- Invitrogen: https://www.thermofisher.com/de/de/home/life-science/antibodies/invitrogen-antibody-validation.html
- LifeTechnologies: https://www.thermofisher.com/de/de/home/life-science/antibodies/invitrogen-antibody-validation/independent-antibody-validation.html
- R&D Systems: https://www.rndsystems.com/tags/antibody-validation
- Sigma-Aldrich: https://www.sigmaaldrich.com/technical-documents/articles/biology/antibody-standard-validation.html

- ApoE, unconjugated, Thermo Fisher, Cat: 701241
https://assets.thermofisher.com/TFS-Assets/LSG/certificate/Certificates-of-Analysis/701241_1984882.PDF

- CD1c-PerCP/Cy5.5, BioLegend, Cat: 331513
https://www.biolegend.com/en-us/global-elements/pdf-popup/percp-cyanine5-5-anti-human-cd1c-antibody-5182?filename=PerCPCyanine55%20anti-human%20CD1c%20Antibody.pdf&pdfgen=true

- CD11b-PE/Cy7, BioLegend, Cat: 101216
https://www.biolegend.com/en-us/global-elements/pdf-popup/pe-cy7-anti-mouse-human-cd11b-antibody-1921?filename=PECy7%20anti-mousehuman%20CD11b%20Antibody.pdf&pdfgen=true

- CD11b-Alexa Fluor 488, BioLegend, Cat: 393107
https://www.biolegend.com/en-us/global-elements/pdf-popup/alexa-fluor-488-anti-human-cd11b-antibody-16010?filename=Alexa%20Fluor%20488%20anti-human%20CD11b%20Antibody.pdf&pdfgen=true

- CD 14 PE-Cy7, BioLegend, Cat: 367111
https://www.biolegend.com/en-us/global-elements/pdf-popup/pe-cy7-anti-human-cd14-antibody-12794?filename=PECy7%20anti-human%20CD14%20Antibody.pdf&pdfgen=true

- CD15-Brilliant Violet 421, BioLegend, Cat: 232039 falsch! ? 323039
https://www.biolegend.com/en-us/global-elements/pdf-popup/brilliant-violet-421-anti-human-cd15-ssea-1-antibody-12371?filename=Brilliant%20Violet%20421%20anti-human%20CD15%20SSEA-1%20Antibody.pdf&pdfgen=true

- CD20-Brilliant Violet 421, BioLegend, Cat: 302329
https://www.biolegend.com/en-us/global-elements/pdf-popup/brilliant-violet-421-anti-human-cd20-antibody-7192?filename=Brilliant%20Violet%20421%20anti-human%20CD20%20Antibody.pdf&pdfgen=true

- CD31-PE, Biolegend, Cat:102507
https://www.biolegend.com/en-us/global-elements/pdf-popup/pe-anti-mouse-cd31-antibody-379?filename=PE%20anti-mouse%20CD31%20Antibody.pdf&pdfgen=true

- CD31-Alexa Fluor 647, Biolegend, Cat: 102516
https://www.biolegend.com/en-us/global-elements/pdf-popup/alexa-fluor-647-anti-mouse-cd31-antibody-3094?filename=Alexa%20Fluor%20647%20anti-mouse%20CD31%20Antibody.pdf&pdfgen=true

- CD45-BrilliantViolet 421, Biolegend, Cat:103133
https://www.biolegend.com/en-us/global-elements/pdf-popup/brilliant-violet-421-anti-mouse-cd45-antibody-7253?filename=Brilliant%20Violet%20421%20anti-mouse%20CD45%20Antibody.pdf&pdfgen=true

- CD45-Alexa Fluor 700, Biolegend, Cat: 368513
https://www.biolegend.com/en-us/global-elements/pdf-popup/alexa-fluor-700-anti-human-cd45-antibody-12399?filename=Alexa%20Fluor%20700%20anti-human%20CD45%20Antibody.pdf&pdfgen=true

- CD45.2-Alexa Flour 700, BioLegend, Cat: 109822
https://www.biolegend.com/en-us/global-elements/pdf-popup/alexa-fluor-700-anti-mouse-cd45-2-antibody-3393?filename=Alexa%20Fluor%20700%20anti-mouse%20CD452%20Antibody.pdf&pdfgen=true
- CD68-Alexa Fluor 594, BioLegend, Cat: 137020
https://www.biolegend.com/en-us/global-elements/pdf-popup/alexa-fluor-594-anti-mouse-cd68-antibody-9671?filename=Alexa%20Fluor%20594%20anti-mouse%20CD68%20Antibody.pdf&pdfgen=true

- CD68-Alexa Fluor 647, BioLegend, Cat: 137004
https://www.biolegend.com/en-us/global-elements/pdf-popup/alexa-fluor-647-anti-mouse-cd68-antibody-6422?filename=Alexa%20Fluor%20647%20anti-mouse%20CD68%20Antibody.pdf&pdfgen=true
- CD68 unconjugated, BioLegend, Cat: 333801
https://www.biolegend.com/en-us/global-elements/pdf-popup/purified-anti-human-cd68-antibody-4835?filename=Purified%20anti-human%20CD68%20Antibody.pdf&pdfgen=true

- CD68 unconjugated, Abcam, Cat: ab955
https://www.abcam.com/cd68-antibody-kp1-ab955.html?productWallTab=Questions

- CD68 -Alexa Fluor 594, R&D systems, Cat: IC20401T https://resources.rndsystems.com/pdfs/datasheets/ic20401t.pdf

- CD115-APC, BioLegend, Cat: 135510

- Claudin 2 unconjugated, Abcam, Cat: ab53032 https://www.abcam.com/claudin-2-antibody-ab53032.html

- Claudin 5 unconjugated, Abcam, Cat: ab15106 https://www.abcam.com/claudin-5-antibody-ab15106.html

- Claudin 13 unconjugated, Invitrogen, Cat: PA1-24420
https://www.thermofisher.com/document-connect/document-connect.html?url=https%3A%2F%2Fassets.thermofisher.com%2FTFS-Assets%2FLSG%2Fcertificate%2FCertificates-of-Analysis%2FMA191114_TA2507851.PDF&title=TG9zLU5yLiZuYnNwO1RBMjUwNzg1MQ==

- Connexin 43 unconjugated, Sigma Aldrich, Cat: C6219 https://www.sigmaaldrich.com/content/dam/sigma-aldrich/docs/Sigma/Datasheet/3/c6219dat.pdf

- CSF1R-APC, Biolegend, Cat: 135510
https://www.biolegend.com/en-us/global-elements/pdf-popup/apc-anti-mouse-cd115-csf-1r-antibody-6336?filename=APC%20anti-mouse%20CD115%20CSF-1R%20Antibody.pdf&pdfgen=true

- CSF1R-Alexa Fluor 647, Biolegend, Cat: 135530
https://www.biolegend.com/en-us/global-elements/pdf-popup/alexa-fluor-647-anti-mouse-cd115-csf-1r-antibody-12485?filename=Alexa%20Fluor%20647%20anti-mouse%20CD115%20CSF-1R%20Antibody.pdf&pdfgen=true

- Donkey anti-Rabbit IgG Alexa Fluor 647, Life Technologies, Cat: A-31573
https://assets.thermofisher.com/TFS-Assets/LSG/certificate/Certificates%20of%20Analysis/1563697_A31573.pdf

- Donkey anti-Rabbit IgG Alexa Fluor 488, Life Technologies, Cat: A-21206
https://www.thermofisher.com/document-connect/document-connect.html?url=https%3A%2F%2Fassets.thermofisher.com%2FTFS-Assets%2FLSG%2Fcertificate%2FCertificates-of-Analysis%2F1644644_A21202.pdf&title=TG9zLU5yLiZuYnNwOzE2NDQ2NDQ=

-E-Cadherin-PE, Biolegend, Cat: 147303
https://www.biolegend.com/en-us/global-elements/pdf-popup/pe-anti-mouse-human-cd324-e-cadherin-antibody-9276?filename=PE%20anti-mousehuman%20CD324%20E-Cadherin%20Antibody.pdf&pdfgen=true

- F4/80-Alexa Fluor 647, BioLegend, Cat: 123122
https://www.biolegend.com/en-us/global-elements/pdf-popup/alexa-fluor-647-anti-mouse-f4-80-antibody-4074?filename=Alexa%20Fluor%20647%20anti-mouse%20F480%20Antibody.pdf&pdfgen=true

- F4/80-FITC, BioLegend, Cat: 123108
https://www.biolegend.com/en-us/global-elements/pdf-popup/fitc-anti-mouse-f4-80-antibody-4067?filename=FITC%20anti-

mouse%20F480%20Antibody.pdf&pdfgen=true
- HLA-DR PE, BioLegend, Cat: 361605
https://www.biolegend.com/en-us/global-elements/pdf-popup/pe-anti-human-hla-dr-antibody-9390?filename=PE%20anti-human%20HLA-DR%20Antibody.pdf&pdfgen=true

- Ki67-AF647, BioLegend, Cat: 652407 https://www.biolegend.com/Default.aspx?Id=18921

- Ly6C-Alexa Flour 488, BioLegend, Cat: 128022
https://www.biolegend.com/en-us/global-elements/pdf-popup/alexa-fluor-488-anti-mouse-ly-6c-antibody-6756?filename=Alexa%20Fluor%20488%20anti-mouse%20Ly-6C%20Antibody.pdf&pdfgen=true
- Ly6G-Brilliant Violet, BioLegend, Cat: 127627
https://www.biolegend.com/en-us/global-elements/pdf-popup/brilliant-violet-421-anti-mouse-ly-6g-antibody-7161?filename=Brilliant%20Violet%20421%20anti-mouse%20Ly-6G%20Antibody.pdf&pdfgen=true

- Ly6G-FITC, BioLegend, Cat: 127606
https://www.biolegend.com/en-us/global-elements/pdf-popup/fitc-anti-mouse-ly-6g-antibody-4775?filename=FITC%20anti-mouse%20Ly-6G%20Antibody.pdf&pdfgen=true

- Ly6G-Alexa Fluor 488, BioLegend, Cat: 127626
https://www.biolegend.com/en-us/global-elements/pdf-popup/alexa-fluor-488-anti-mouse-ly-6g-antibody-7085?filename=Alexa%20Fluor%20488%20anti-mouse%20Ly-6G%20Antibody.pdf&pdfgen=true

- Ly6G-Alexa Fluor 647, BioLegend, Cat: 127610
https://www.biolegend.com/en-us/global-elements/pdf-popup/alexa-fluor-647-anti-mouse-ly-6g-antibody-4780?filename=Alexa%20Fluor%20647%20anti-mouse%20Ly-6G%20Antibody.pdf&pdfgen=true

- MHC II-PE, Biolegend, Cat: 107608
https://www.biolegend.com/en-us/global-elements/pdf-popup/pe-anti-mouse-i-a-i-e-antibody-367?filename=PE%20anti-mouse%20I-AI-E%20Antibody.pdf&pdfgen=true

- Trem 2 unconjugated, Abcam, Cat: ab86491 https://www.abcam.com/trem2-antibody-rm0139-5j46-ab86491.html

- Trem2-APC, R&D systems, Cat: FAB17291A https://resources.rndsystems.com/pdfs/datasheets/fab17291a.pdf

- ZO-1 unconjugated, EMD Millipore, Cat: AB2272
http://www.merckmillipore.com/DE/de/product/Anti-ZO-1-Antibody,MM_NF-AB2272?ReferrerURL=https%3A%2F%2Fwww.google.com%2F#documentation

Animals and other organisms

Policy information about studies involving animals; ARRIVE guidelines recommended for reporting animal research

Laboratory animals

In this study the following mouse lines were used:

- C57BL/6
Strain: C57BL/6J, Source: Charles River, Identifier: 632

- C57BL/6
Strain: C57BL/6JRj, Source: Janvier Labs

- Cx3cr1cre:R26-tdTomato
Strain: Tg(Cx3cr1-cre)MW126Gsat/Mmucd, Source: MMRRC, Identifier: 036395-UCD

- DsRed
Strain: STOCK Tg(ACTB-DsRed*MST)1Nagy/J, DsRed.T3, Source: The Jackson Laboratory, Identifier: 005441

- Cx3cr1creER
Strain: B6.129P2(C)-Cx3cr1tm2.1(cre/ERT2)Jung/J, Source: The Jackson Laboratory, Identifier: 020940

- CSF1RcreER
Strain: FVB-Tg(Csf1r-cre/Esr1*)1Jwp/J, Source: The Jackson Laboratory, Identifier: 019098

- iDTR
Strain: C57BL/6-Gt(ROSA)26Sortm1(HBEGF)Awai/J, Source: The Jackson Laboratory, Idnetifier: 007900

- tdTomato
Strain: B6;129S6-Gt(ROSA)26Sortm9(CAG-tdTomato)Hze/J, Source: The Jackson Laboratory, Identifier: 007905

- CD115DTR
Strain: C57BL/6-Tg(Csf1r-HBEGF/mCherry)1Mnz/J, Source: The Jackson Laboratory, Identifier: 024046

- Cx3cr1gfp
Strain: B6.129P-Cx3cr1tm1Litt/J, Source: The Jackson Laboratory, Identifier: 005582

	All mice were housed under "specific pathogen-free" (SPF) conditions at the animal facilities of the University of Erlangen, Germany. Male and female mice at an age of 8-18 weeks were used.
Wild animals	This study does not include wild animals.
Field-collected samples	This study does not include field-collected samples.

Human research participants

Policy information about studies involving human research participants

Population characteristics	Synovial biopsies were obtained from knee joints of patients diagnosed with osteoarthritis (OA) and rheumatoid arthritis (RA), respectively. RA patients fulfilled the 2010 EULAR/ACR criteria of RA. All patients were ≥ 18years of age.
Recruitment	OA patients were recruited at the Department of Trauma Surgery, Universitätsklinikum Erlangen and RA patients were recruited at the Department of Internal Medicine 3 - Rheumatology and Immunology, Universitätsklinikum Erlangen. All patients signed an informed consent.

Flow Cytometry

Plots

Confirm that:

☒ The axis labels state the marker and fluorochrome used (e.g. CD4-FITC).

☒ The axis scales are clearly visible. Include numbers along axes only for bottom left plot of group (a 'group' is an analysis of identical markers).

☒ All plots are contour plots with outliers or pseudocolor plots.

☒ A numerical value for number of cells or percentage (with statistics) is provided.

Methodology

Sample preparation	Sample preparation is described in detail in the supplemental experimental procedures.
Instrument	Flow cytometry was performed with a CytoFLex S, Beckman Coulter. Sorting of cells was performed with a MoFlo XDP, Beckman Coulter.
Software	Flow cytometry data and cell sorting data were analyzed via the Summit Software System, CytExpert, FlowJo, and Kaluza software.
Cell population abundance	Purity of sorted cells was confirmed by flow cytometry analysis.
Gating strategy	FACS strategies are provided in detail in the extended data and supplementary experimental procedures.

☒ Tick this box to confirm that a figure exemplifying the gating strategy is provided in the Supplementary Information.